

3-26-2015

Analysis of Muon Induced Neutrons in Detecting High Z Nuclear Materials

Logan J. Brandt

Follow this and additional works at: <https://scholar.afit.edu/etd>

Recommended Citation

Brandt, Logan J., "Analysis of Muon Induced Neutrons in Detecting High Z Nuclear Materials" (2015).
Theses and Dissertations. 76.
<https://scholar.afit.edu/etd/76>

This Thesis is brought to you for free and open access by the Student Graduate Works at AFIT Scholar. It has been accepted for inclusion in Theses and Dissertations by an authorized administrator of AFIT Scholar. For more information, please contact AFIT.ENWL.Repository@us.af.mil.



**Analysis of Muon Induced Neutrons in
Detecting High Z Nuclear Materials**

THESIS

Logan J. Brandt, Second Lieutenant, USAF

AFIT-ENP-MS-15-M-109

**DEPARTMENT OF THE AIR FORCE
AIR UNIVERSITY**

AIR FORCE INSTITUTE OF TECHNOLOGY

Wright-Patterson Air Force Base, Ohio

Approved for public release; distribution unlimited

The views expressed in this document are those of the author and do not reflect the official policy or position of the United States Air Force, the United States Department of Defense or the United States Government. This material is declared a work of the U.S. Government and is not subject to copyright protection in the United States.

AFIT-ENP-MS-15-M-109

ANALYSIS OF MUON INDUCED NEUTRONS IN DETECTING HIGH Z
NUCLEAR MATERIALS

THESIS

Presented to the Faculty
Department of Engineering Physics
Graduate School of Engineering and Management
Air Force Institute of Technology
Air University
Air Education and Training Command
in Partial Fulfillment of the Requirements for the
Degree of Master of Science

Logan J. Brandt, BS
Second Lieutenant, USAF

March 2015

Approved for public release; distribution unlimited

ANALYSIS OF MUON INDUCED NEUTRONS IN DETECTING HIGH Z
NUCLEAR MATERIALS

THESIS

Logan J. Brandt, BS
Second Lieutenant, USAF

Committee Membership:

Dr. Larry W. Burggraf, PhD
Chairman

Dr. Justin A. Clinton, PhD
Member

Maj Gregory K. Van Dyk, PhD
Member

Abstract

Simulations of muon interactions with high Z material using two different muon energies, 100 MeV and 1 GeV, were performed on five different materials of various atomic numbers yielding average neutron production rates that range from 2.3 ± 0.01 in enriched uranium to negligible amounts in aluminum when exposed to the 100 MeV energy muons. As the muon energy was increased to 1 GeV, neutron yields shrank to negligible levels. Little difference was found in neutron yield produced in non-fissile material.

Experimental data was collected by exposing a 15 cm thick block of iron, and 5 and 15 cm thick blocks of lead to the natural atmospheric muon flux. The incident muon energy distribution was found to have a mode of 180 MeV and a mean of 520 MeV. Probability distributions were constructed for the neutron yields of each incident muon and no difference was found in the various distributions. The average muon induced neutron yield was also calculated and found to be 3.4 ± 0.1 for a 15 cm thick block of iron, 2.8 ± 0.1 for a 5 cm thick block of lead, and 2.2 ± 0.1 for a 15 cm thick block of lead.

Table of Contents

	Page
Abstract	iv
List of Figures	vii
List of Tables	x
I. Introduction	1
1.1 Objective	1
1.2 Motivation	2
II. Theory	4
2.1 Muon Imaging	5
2.2 Muon Induced Fission	8
Prompt Muon Induced Fission	9
Delayed Muon Induced Fission	10
2.3 Muon Catalyzed Fusion	11
2.4 Muon Spallation	11
2.5 Neutron Detectors	12
2.6 Muon Detection	15
III. Methodology	19
3.1 Overview	19
3.2 Experimental Setup	19
Muon Detection	19
Neutron Detection	22
Digitizer Synchronization	24
IV. Results and Analysis	26
4.1 Modeling Results	26
Initial Modeling	26
Final Modeling	30
4.2 Experimental Results	33
Muon Energy Determination	33
Neutron Yield Analysis	35
Energy Dependent Neutron Yield	38

	Page
V. Conclusions	42
5.1 Research Summary	42
5.2 Future Work	43
Appendix A. PHA Software Settings	45
Appendix B. PSD Software Settings	46
Appendix C. Neutron Detector Voltages	47
Appendix D. NaI(Tl) Detector Calibration	48
Appendix E. Matlab Code	51
Bibliography	100

List of Figures

Figure	Page
1 Diagram of muon creation through cosmic ray interaction in the atmosphere.	4
2 Cosmic muon imaging results provided the density measurements for the lava dome.	6
3 Muon Tomography experiment setup performed at CERN imaging lead blocks.	7
4 Muon Tomography experiment results performed at CERN imaging lead blocks.	7
5 The cycle of muon catalyzed fusion for a deuterium-deuterium reaction	12
6 Feynman diagram depicting neutron production through the exchange of a virtual photon between a muon and a nucleus.	13
7 A 2D Histogram of PSD values shows the difference between neutron and gamma energy depositions within the liquid scintillators.	14
8 Stopping power of copper for a range of incident muon energies	17
9 Energy deposition curve according to the Bethe-Block equation for a NaI(Tl) scintillation detector	18
10 A depiction of the experimental setup used for this experiment.	20
11 The muon coincidence and energy determination portion of the experimental setup.	21
12 One ring composed of six liquid scintillators.	22
13 Neutron detector array composed of four rings of six detectors apiece.	23
14 PSD 2D histogram used to determine neutron discrimination cut lines.	24

Figure		Page
15	Clock synchronization method utilizing a function generator.	25
16	Geometry setup for the Geant4 simulation modeling muon induced neutrons.	27
17	Muon energy spectrum after being moderated by 30 cm of concrete.	28
18	Muon induced fission neutron energy spectrums from four different materials produced using 100 MeV muons.	28
19	Muon induced fission neutron energy spectrums from four different materials produced using 1 GeV muons.	29
20	Geometry setup for a Geant4 simulation modeling muon induced neutrons in a 5 cm thick lead target.	31
21	Dependence of average neutron yield on muon energy for four different material and geometry configurations.	32
22	Incident Muon Energy Distribution	35
23	Total neutron yields acquired for all materials over their respective seven day runs.	36
24	Neutron yield distribution produced above background levels	37
25	Neutron count probability distribution.	38
26	Scatter plot showing neutron yield and muon energy for each incident muon	39
27	Average neutron yields for each incident muon energy.	40
28	Incident muon energy spectra for various neutron yields.	41
29	Computer software settings for pulse height analysis of the NaI(Tl) detectors.	45
30	Computer software settings for pulse shape discrimination and neutron detection.	46
31	Pulse height distribution for pulse heights measured during experiments.	49

Figure	Page
32 NaI(Tl) calibration curves.	50

List of Tables

Table	Page
1 Average Neutron Yield per Muon For Initial Simulation	30
2 Average Neutron Yield per Muon For Final Simulation	32
3 Mean neutron yields per muon after 7 days of exposure	37
4 Voltage settings for the various liquid scintillation neutron detectors.	47

ANALYSIS OF MUON INDUCED NEUTRONS IN DETECTING HIGH Z NUCLEAR MATERIALS

I. Introduction

1.1 Objective

Currently a need exists to detect shielded special nuclear material using passive interrogation techniques. Muon imaging holds the potential to satisfy this requirement, but current implementations are hindered by long detection times. A proposed solution is to utilize neutrons produced by muon interactions with the fissile material to supplement current muon imaging techniques. It is predicted that muon induced fission of fissile nuclear materials will produce enough detectable neutrons through interactions within the target that resulting signals can be utilized as an additional detection method when neutrons are detected in coincidence with incoming muons.

The primary objective of this research is to examine the neutron production rate of various materials when exposed to atmospheric muons. As not all material contained within a nuclear weapon is fissile, it is important to understand the neutron production capabilities of a wide range of atomic number elements. It is anticipated that the actinide elements, especially fissile actinides which have a low activation energy for fission, will produce a higher number of neutrons through muon induced fission events, while neutron production will decrease for the lower Z materials. This research will focus on the muon induced neutron production from both iron and lead.

1.2 Motivation

Accurate detection of Special Nuclear Material (SNM) is of paramount importance to issues of national security and international treaty verification. With the rise of non-state actor terrorist organizations, a fear of a nuclear weapon falling into the hands of one of these organizations and being smuggled into the United States has become more viable. This fear has prompted the Department of Homeland Security (DHS) and Department of Defense (DoD) to work with the Department of Energy (DoE) laboratories to create detection portals for use at locations such as border crossings and harbors. These portals utilize detectors such as thallium doped sodium iodide (NaI(Tl)) scintillation detectors and High Purity Germanium (HPGe) detectors to indirectly inspect incoming vehicles and/or shipping containers for any type of potential nuclear material or Radiological Dispersion Device (RDD). However, these detection methods can be defeated with ample shielding of the smuggled material. If surrounded by enough material at a high atomic number, the gamma rays can be sufficiently attenuated to undetectable levels.

Moreover, as the nuclear arsenals of the major nuclear weapon states continue to decrease, the need arises for more accurate verification methods of the material contained within these weapons. Visual inspections and active interrogation techniques are prohibited, due to the possibility of revealing sensitive weapon design information. Additionally, thick outer casing material can have the same shielding problem in the portal scenario. Since active examination of internal components are not allowed, an alternate method of imaging and detecting special nuclear material is required. Muon imaging has been suggested as one solution to this problem [1].

Muon tomography utilizes negatively charged muons created by cosmic particle interactions in the upper atmosphere. These particles are 207 times more massive than an electron and have a mean lifetime of $2.2 \mu\text{s}$ [2]. Because of their capability to

penetrate through dense materials, muons have been used to image major geographical landmarks. In one instance they were utilized to examine the magma buildup in an active volcano located in Japan [3]. In another, researchers capitalized on the muon's penetration capability to examine the pyramids for hidden chambers [4]. A similar technique could be applied to weapons inspection procedures to probe the unobservable physics package for dense nuclear fuel even in the presence of dense shielding material.

When muon tomography alone is used, the time period required for the necessary resolution of meaningful information is on the order of tens of hours [5]. However, it may be possible to decrease the detection time of nuclear material if muon tomography is combined with neutron detection from muon induced fission. In this process, a muon may interact with a heavy nucleus and replace an electron in the atom. As the muon deexcites and is captured by the heavy nucleus, it has a chance to transfer its energy to the nucleus which can be enough to overcome the fission activation barrier if the fission barrier is low. These fission events produce excess neutrons in the system which can be detected and utilized in further analysis of the system under examination.

II. Theory

As stated previously, muons are subatomic particles known as leptons with a mass 207 times that of the electron and can have either a positive or negative charge. They are primarily produced in the upper atmosphere through collisions of cosmic rays, predominately very energetic protons, and the atmospheric molecules. As these high energy protons collide with other particles, pions are produced which quickly decay into both positive and negative muons [6]. These are much longer lived, with a mean lifetime of $2.2 \mu\text{s}$. Since they are created at such high energies and, thus having relativistic velocities, these particles can easily reach the surface of the earth to interact with matter there. An example of this creation process can be seen in Figure 1. These muons will reach the surface at a rate of approximately 10,000 muons/min/m².

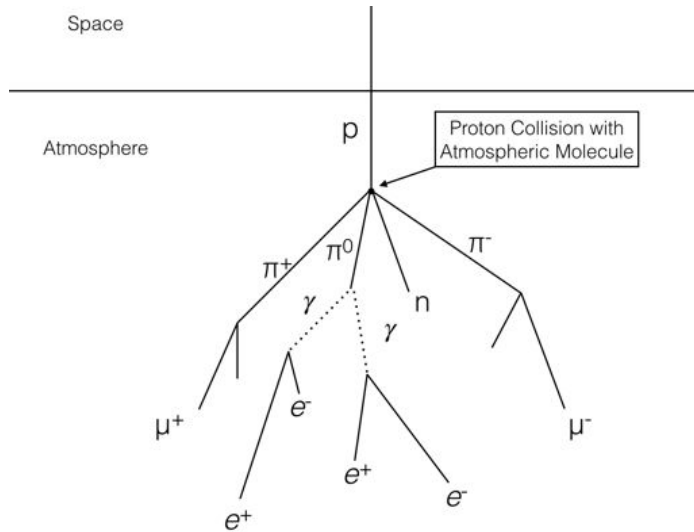


Figure 1. High energy collisions of cosmic ray protons in the upper atmosphere will produce pions that quickly decay into muons among other particles.

2.1 Muon Imaging

Because of the nearly constant muon flux, these naturally occurring muons have been used to image various objects since the early 1970s. At that time Alvarez et al. capitalized on the muons ability to penetrate through large amounts of material by imaging Cepherens pyramid [4]. In this particular experiment, the inspecting team placed detectors beneath the desired location to be inspected and gathered data for several months. Once the exposure was completed, the detected muon flux was compared to the known background levels. By accounting for the anticipated attenuation of the muons in the density of material overhead, the internal structure of the pyramid could be mapped out to rule out the possibility of a hidden chamber within Cepherens pyramid which had been previously found in others.

In another similar experiment, Tanaka, et al. placed one 4000 cm^2 AgBr emulsion cloud chamber located underground approximately 1 km away from the Asama volcano in Japan to gather density data [3]. To confirm the accuracy of their findings, the team then imaged the Usu lava dome and compared to other known density measurements. These findings can be seen in Figure 2. This same technique has also been suggested for application in imaging damaged nuclear reactors such as Fukushima, that it would be unsafe to approach and inspect at a close distance [7] [8].

In both of these illustrations, the muon imaging was conducted over very long periods of time to observe a sufficient decrease in the muon flux due to attenuation in the dense material. Two other forms of muon imaging also exist. Muon tomography works by measuring the amount of scattered muons. Two detectors are placed on either side of the object, one to measure the incoming angle of the muon, and another to measure the exiting direction. Since muons are much more likely to scatter at a greater angle when passing through dense material, an idea of the location of the material in between the two detectors can be gathered. In 2007 an experiment was

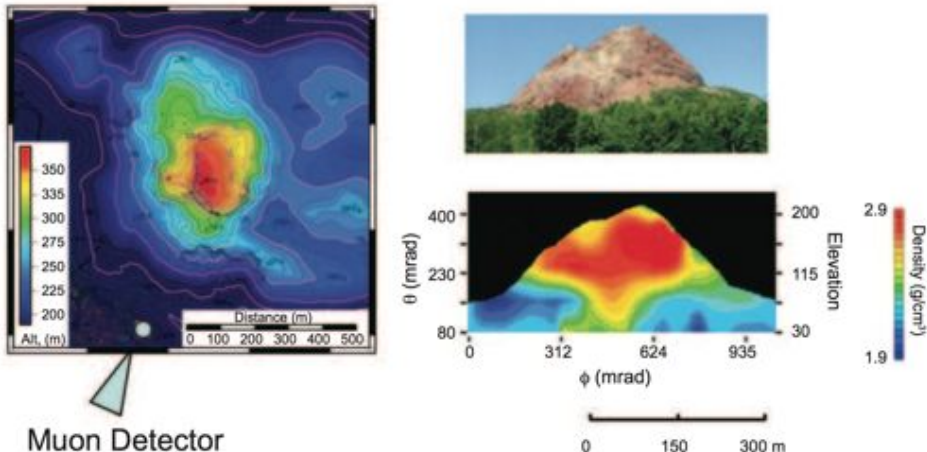


Figure 2. Cosmic muon imaging results provided the density measurements for the lava dome. Alternate density measurements were available and confirmed the accuracy of the muon imaging technique. [3] This image has been reproduced with the permission of the American Journal of Science.

conducted at CERN to examine this very technique. In the experiment, two lead blocks were placed between gas filled drift tubes in the setup seen in Figure 3 [9]. The results of the CERN experiment can be seen in Figure 4.

Further studies have been conducted using this same technique and have produced promising results. The DOE has even worked with Decision Sciences International Corporation to develop portal systems which have been shown to clear a cargo container in approximately 30 seconds [10].

Another method of muon imaging is known as telescopic mode. In this method, it is only necessary to detect incoming muons. Of all the muons that enter the material, some will be moderated to a point that they will stop and be captured within the target material. At this point, secondary signals can be given off which can be detected to confirm the presence of various types of material. To confirm the presence of nuclear material specifically, a secondary signal must be acquired through either gamma or neutron production via muon induced fission events. Several studies have been conducted to examine the feasibility of this particular method and have

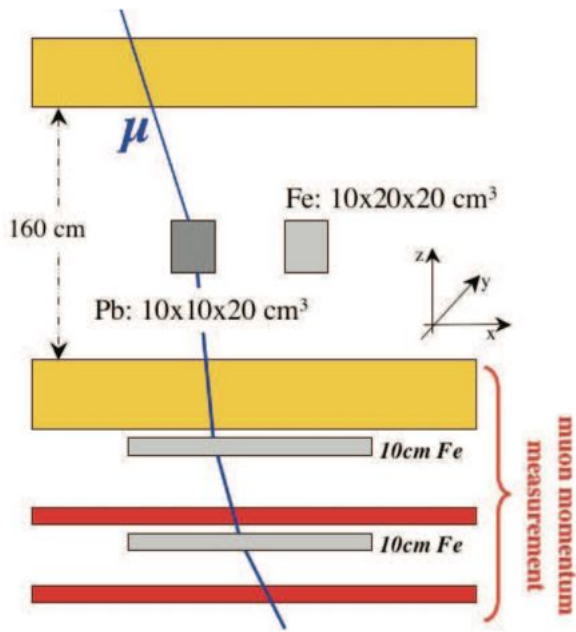


Figure 3. Experimental setup utilized in the muon tomography experiment run by CERN when inspecting the location of two lead blocks. [9] Copyright (2007) IEEE

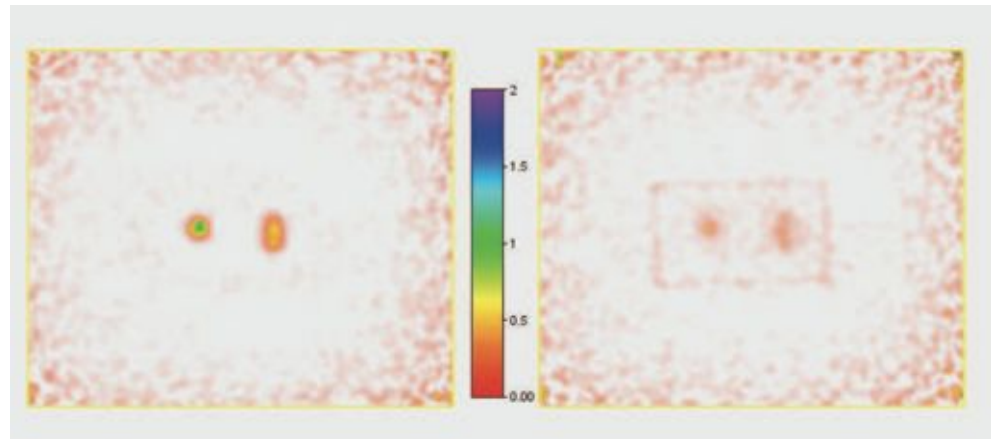


Figure 4. Experimental results demonstrate muon tomography's capability to detect and determine location of lead blocks. [9] Copyright (2007) IEEE

shown much promise [6]. It is this type of muon imaging, telescopic mode, that will be the focus of this experiment.

It should be noted that muon tomography and telescopic mode are not mutually exclusive. In fact, they may be complimentary to one another based upon the muon energy dependence of the phenomena. High energy muons primarily interact at a localized point via scattering events which can be utilized through scattering tomography. Lower energy muons have a much higher linear energy transfer making moderation within the material much more probable and increasing the effectiveness of neutron production and gamma emission. By using both methods simultaneously, more information can be gathered about the target material than by using one method exclusively.

2.2 Muon Induced Fission

Fission occurs when a nucleus is imparted with enough energy to overcome the strong nuclear force holding its nucleons together. When this occurs, the nucleus will split into two daughter nuclei and several neutrons, and the masses of the individual components will sum to less than that of the original. This change in mass is released as energy according to the equation, $E = mc^2$. The fission phenomenon is well understood by the scientific community and has been utilized in both the creation of weapons and power plants for energy production.

Muon Induced Fission (μ IF) was originally proposed by Wheeler in 1948 [11]. Since that time it has been explored in much more depth and has proven useful in studying nuclear energy dissipation and fission dynamics [12] [13]. μ IF occurs by two processes, by electromagnetic radiationless transition causing prompt fission or by weak capture reactions causing delayed fission. In both cases, it is important to note the time scales of muon capture occur on timescales that are small compared to

the mean lifetime of the muon itself [14] [15]. This allows the muons to be captured by the material and transfer the energy to a nucleus. If the energy transfer is large enough, the fission barrier can be overcome and the nucleus will split. Alternatively, if the energy transfer is not sufficient for fission, the muon can be captured by a proton within the nucleus, converting the atom to another element.

To initiate the fission process, a negatively charged muon must first interact with the material. As the muon enters the fissionable material and begins to interact through collisions, it rapidly loses a majority of its energy by ionizing the surrounding material within 10^{-9} to 10^{-10} s [15]. This process may continue until enough time has passed and the muon eventually reaches the end of its lifetime. When this occurs, the negative muon will decay into a muon neutrino, an electron, and an electron neutrino, and the reaction can be seen in Equation 1.



Because the muon decay process is slow compared to the processes under consideration, its effects are negligible. An alternative to this scenario occurs with the capture of a muon. In such an event, the muon will replace an electron in one of the outer electron orbitals forming an excited muonic atom [15]. From this position, μ If in both prompt and delayed processes may occur.

Prompt Muon Induced Fission.

In the case of μ If, prompt fission occurs through the energy transfer of the muons' transitions within the atomic energy levels. Because a muon acts as a heavy electron, its behavior can be thought of in an analogous manner. Once captured the muon will reside in the outer orbitals of the atom until it deexcites to one of the lower energy levels. The $2p - 1s$ and $3d - 1s$ transitions are on the order of the fission barrier in the

actinide elements [16] [15]. In these situations, the energy can be transferred directly to the nucleus rather than expelled from the atom via electromagnetic radiation in a process known as inverse internal conversion [15]. After such an event has taken place, the nucleus will be imparted with enough energy to exceed the fission barrier. The nucleus will split and, most often, the muon will remain attached to the larger fission fragment. However, it has been observed that under certain circumstances the muon will attach to the lighter fission fragment. In such case the muon attachment rates to the lighter daughter product can be examined as an analysis tool to study the prompt fission dynamics [15].

Delayed Muon Induced Fission.

Delayed μ IF requires the muon to have been captured within the atomic orbitals and to have decayed into the ground state. In this configuration the muon will spend a significant portion of its time residing inside the nucleus due to its excessive mass. At that location, the muon can be captured by a proton resulting in a neutron and a muon neutrino. This process yields an average nucleus excitation energy of 15-20 MeV which is much greater than the actinide fission barrier of 5-6 MeV [15]. Such a large energy transfer has the ability to allow for secondary or even higher fission events [16]. It should be noted that the mean lifetime of these events is based upon the weak decay process on the order of $10^{-8}s$ [15]. As these timescales are two orders of magnitude less than the muon lifetime, muon decay can be neglected in describing the fission processes. Measurements have been made of the daughter mass distributions, delayed fission probabilities, and prompt to delayed fission ratios [16].

2.3 Muon Catalyzed Fusion

Fusion occurs when two light nuclei combine to form one larger nucleus with a mass less than the sum of the original components. The difference in mass is released as energy and can be calculated using Einstein's equation, $E = mc^2$. In practice, fusion is difficult to achieve due to the highly repulsive Coulombic force of both positively charged nuclei. Typically, fusion reactions require high temperatures, laser stimulation, and magnetic confinement.

However, fusion of heavy hydrogen isotopes can be achieved without the need for these high temperatures or laser stimulation by way of Muon Catalyzed Fusion (μ CF). In this process, a heavy negatively charged muon replaces the electron. The muon resides between two hydrogen isotopes and masks the coulomb barrier thereby reducing the atom's radius by over 200 times that of a normal hydrogen molecule from approximately 10^{-8} cm to 5.1×10^{-11} cm. [17] [18] The reduction in size enables higher rates of quantum tunneling of one nucleus through the coloumb barrier of the other resulting in a fusion event. This technique was first proposed by Andrei Sakharov and F.C. Frank in 1947 and has since been proven experimentally [19]. The most common fusion reactions are those of Deuterium-Deuterium (DD) and Deuterium-Tritium (DT), with the cross section for the DT molecule approximately 100 times larger than the DD molecule [20] [21] . The entire cycle for deuterium-deuterium fusion can be seen in Figure 5.

2.4 Muon Spallation

A third means of muon neutron production is via muon spallation. In this method, the incoming muon exchanges a virtual photon with the interaction nucleus. This interaction can provide the nucleus with enough energy to emit one or several neutrons. The Feynman diagram in Figure 6(a) demonstrates this process [22]. It is the main

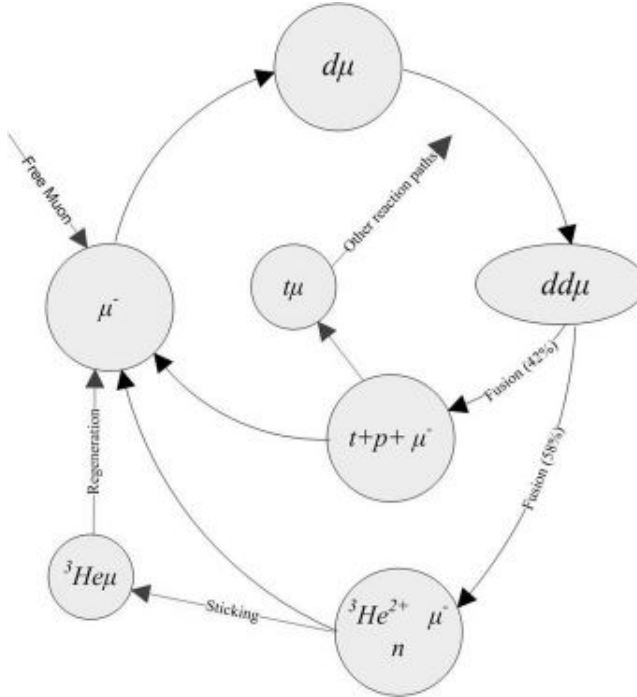


Figure 5. The cycle of muon catalyzed fusion for a deuterium-deuterium reaction. Reproduced from Dr. Van Dyk's dissertation. [1]

contribution to background noise in deep underground experiments searching for dark matter and neutrinoless double beta decays [23].

2.5 Neutron Detectors

In order to properly associate neutron events with an incident muon, it is necessary to construct a system in which the produced neutrons can be counted in coincidence with a muon event. To accomplish this objective, a nearly 4π solid angle neutron detection system should be implemented to produce maximum efficiency of neutron detection. It should have the capability to discriminate between neutrons and gamma events and also have a high probability of interaction. All three of these objectives can be accomplished using neutron/gamma discriminating liquid scintillators. Detectors like the BC-501A/EJ-301 and BC-519/EJ-309 can be formed into the desired configuration in order to gain as close to 4π coverage as possible while simultaneously

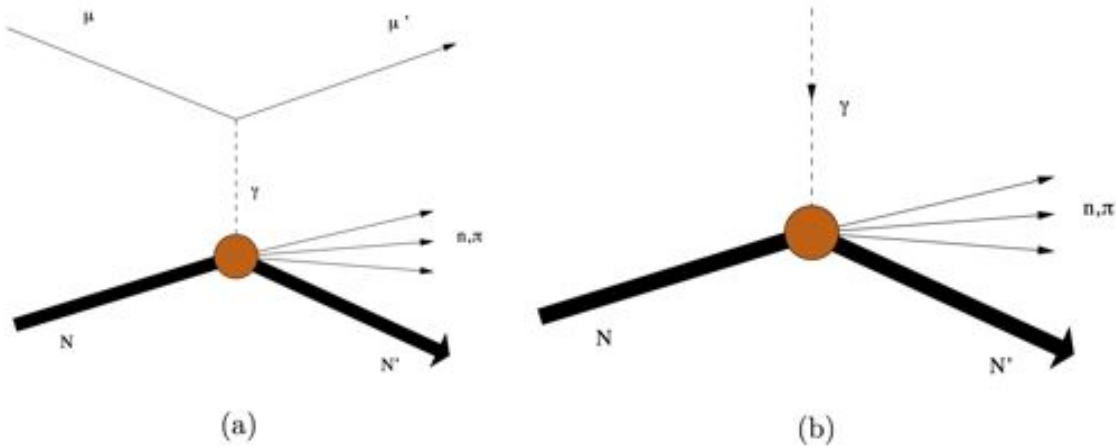


Figure 6. (a)Feynman diagram depicting neutron production through the exchange of a virtual photon between a muon and a nucleus. (b)Feynman diagram displaying neutron production through photon absorption. Reproduced from Lawrence Livermore National Laboratory's report on Neutron Production by Muon Spallation. [22]

providing the capability to discriminate between neutron events and gamma events by way of the detection method. Neutron events are detected through recoil proton collisions in the hydrogen present within the scintillation material. These recoil protons have a decay time which is much longer than a gamma interaction within the same material. These decay times are associated with a Pulse Shape Discrimination (PSD) value by integrating the charge collected in two different time characteristics of the pulse, Q_{short} and Q_{long} . Both of these charge integrations begin at the trigger point, and can then be used to calculate the PSD value by using Equation 2.

$$PSD = \frac{Q_{long} - Q_{short}}{Q_{long}} \quad (2)$$

By plotting a 2D Histogram of the PSD values calculated by electronic digitizers after the exposure of the detectors to a neutron source, such as a plutonium beryllium source, the difference in PSD values for neutrons and gammas can be utilized to distinguish between neutron and gamma detections. An example plot can be seen in Figure 7. Once a similar plot has been produced, cut lines can be determined

to filter out the extraneous information produced from gamma detection to ensure that only neutron events are counted in coincidence with incident muons within the detection system. PSD firmware, such as that produced by Caen S.p.A, is utilized to accomplish all these tasks. It should also be noted that there is an overlap of the PSD values for neutrons and gammas at low energies. This overlap is not entirely removed when only a single cut criterion is applied.

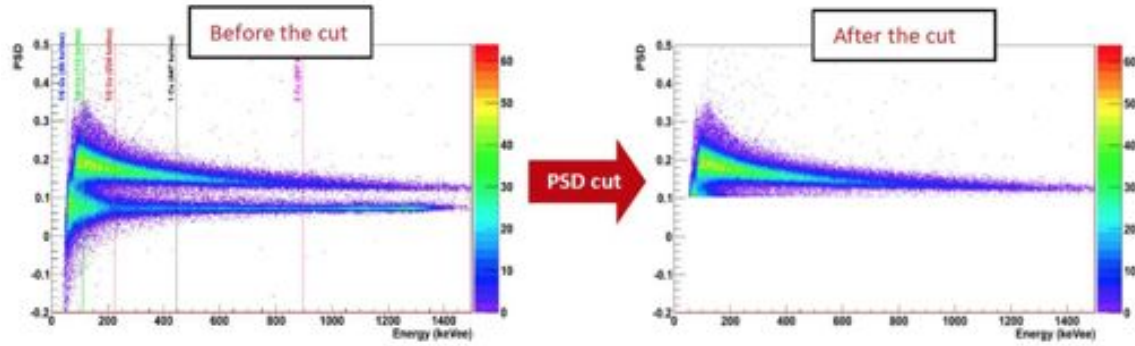


Figure 7. A 2D Histogram of PSD values shows the difference between neutron and gamma energy depositions within the liquid scintillators. [1]

Detection efficiency also must be considered when arranging the liquid scintillators. The arrangement must maximize the absolute detector efficiency which considers the geometry of the setup as well as the intrinsic efficiency of the detector itself. The geometry component is determined by the solid angle of the source exposed to the detector when compared to a solid angle of 4π . If a right cylindrical detector is considered and a point source is located on the axis, the solid angle, Ω , can be calculated using Equation 3.

$$\Omega = 2\pi \left(1 - \frac{d}{\sqrt{d^2 + a^2}} \right) \quad (3)$$

In Equation 3, d is the distance front the source to the detector and a is the radius of the detector. The other component of absolute efficiency is the detectors intrinsic efficiency. Intrinsic efficiency takes into account how many of the neutrons

that make it to the detector are actually detected by the detector in question. It can be calculated using Equation 4,

$$\epsilon_{int} = \frac{N_H \sigma_H}{N_H \sigma_H + N_C \sigma_C} (1 - e^{-(N_H \sigma_H + N_C \sigma_C)d}) \quad (4)$$

In Equation 4, N is the number density of atoms in the detector per cm³, σ is the scattering cross section of the given element, and d is the distance traveled by the neutron [24]. Once the intrinsic efficiency and the geometry are known, the absolute efficiency can be calculated using Equation 5.

$$\epsilon_{abs} = \epsilon_{int} \frac{\Omega}{4\pi} \quad (5)$$

2.6 Muon Detection

Muon detection is a vital component to any muon imaging system and, therefore, must be considered in depth. To properly associate a given neutron detection with an incident muon, the muon must first be detected and verified as a muon. It has been proposed to utilize a series of NaI(Tl) scintillation detectors to accomplish this task [1]. In such a method, the incident particle will deposit energy in the detectors which can then be utilized to both confirm the presence of an incoming muon and provide a means of energy determination. Muons with energies greater than several keV will lose a portion of their energy within the detectors through ionization processes and produce a linear energy transfer characterized by the Bethe-Block equation (Equation 6) [25].

$$-\frac{dE}{dx} = 4\pi N_a r_e^2 c^2 \rho \frac{Z}{A} \frac{1}{\beta^2} \left[\frac{1}{2} \ln \left(\frac{2m_e c^2 \gamma^2 \beta^2 T_{max}}{I^2} \right) - \beta^2 - \frac{\delta}{2} \right] \quad (6)$$

where

$$T_{max} = \frac{2m_e c^2 \beta^2 \gamma^2}{1 + \frac{2\gamma m_e}{m_{part}} + \left(\frac{m_e}{m_{part}}\right)^2} \quad (7)$$

$$\delta = 2 \log_{10} x - \bar{C} + a (x_1 - x)^k \quad (8)$$

and

$$x = \log_{10} \frac{p}{m_{part} c} \quad (9)$$

The variable r_e is the electron radius, 2.187×10^{13} m; m_e is the electron mass, 9.109×10^{-31} kg; m_{part} is the particle mass; N_a is Avagadro's number of 6.022×10^{23} atoms/mol; I is the mean ionization potential in MeV; Z is the proton number; A is the atomic mass; ρ is the material density; $\beta = v/c$ where v is the velocity of the particle and c is the speed of light; γ is the relativistic constant; and p is the particle's momentum. In each equation the energy is supplied in MeV and masses are supplied in MeV/c². \bar{C} , a , x_1 , and k are all unitless fitting parameters for a given material which have been tabulated [26]. The final curve for a muon incident upon a piece of copper material is shown in Figure 8.

The Bethe-Block equation can be used in conjunction with Equation 10, where ρ is the material density and R is the distance traveled in the material, to find the energy deposited within a certain material. These calculations can be applied to find an incident muon energy by using a detector that has the capability to measure deposited energy within the material.

$$Energy Deposited = \rho \int_0^R -\frac{dE}{dx} dx \quad (10)$$

Such a case applies for utilizing NaI(Tl) detectors. A muon's energy deposition curve has been plotted in Figure 9 for negative muon in a NaI(Tl) detector. As can be seen, the energy deposition varies with incident muon energy, and thus, the muon

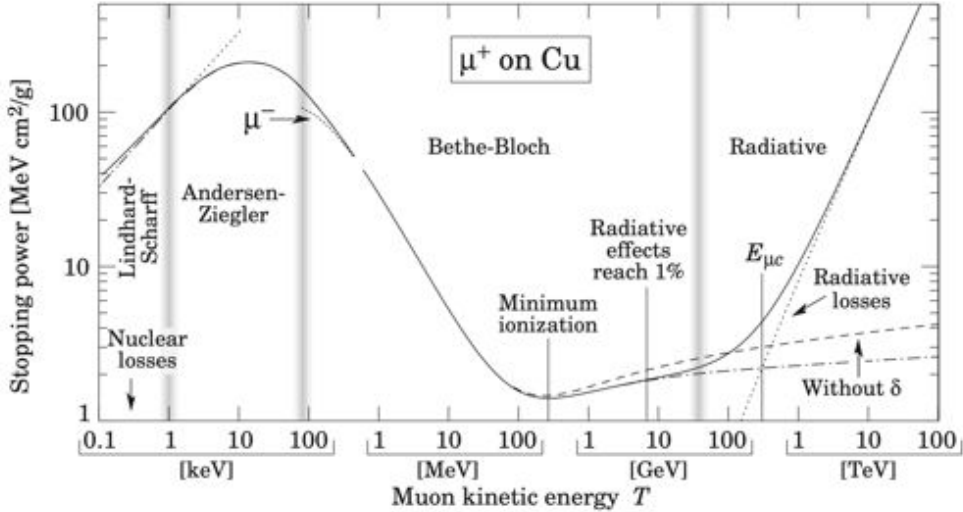


Figure 8. The plot displays the linear energy transfer for muons passing through copper material for various incident muon energies. Copyright (2001) Academic Press [25]

energy can be calculated based upon the detector response. By only considering events that deposit energies of anticipated values, many sources of background radiation may be eliminated. This method can then be utilized to verify that the detectors have detected a muon instead of other sources.

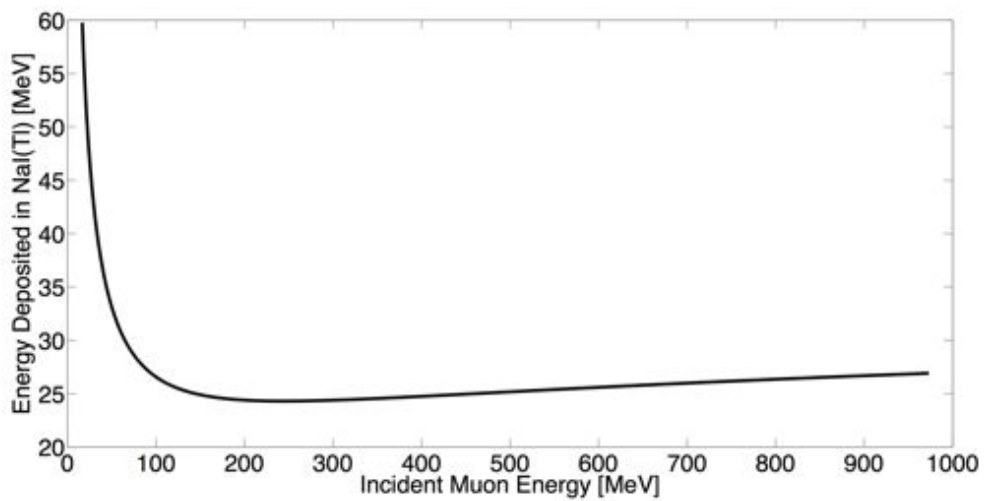


Figure 9. The plot displays the energy deposited in a NaI(Tl) scintillation detector based on the incident muon energy. All data has been calculated according to the Bethe-Block equation. Reproduced from Dr. Van Dyk's dissertation. [1]

III. Methodology

3.1 Overview

In order to conduct this experiment, a setup was created in which incoming muons were detected in coincidence with neutrons produced by muon interactions within two materials, iron and lead. To accomplish such a task, an experimental design laid out by Dr. Van Dyk was utilized. The proposed setup featured a novel muon funnel that directs cosmic muons through various scattering angles and has been shown to increase the muon flux by 3% through a given area [1]. Immediately below this funnel, a series of four NaI(Tl) scintillation detectors were used to determine the presence of a muon and it's incident energy on the system. After passing through the NaI(Tl) detectors, the muon then entered the desired material to be studied. The experiment was surrounded with 24 EJ-309 pulse shape discriminating liquid scintillators. These detectors provided a method to detect the desired neutron products and also allowed pulse shape discrimination to be applied to the signal in order to ignore any extraneous gamma signals that were detected. The entire detection setup below the funnel assembly can be seen in Figure 10.

3.2 Experimental Setup

Muon Detection.

The muon detection system served to both detect incoming muons in coincidence with the produced neutrons, and also to determine the incident muon energy to analyze any energy dependence of the neutron output. To accomplish this objective, four NaI(Tl) scintillation detectors, 5.08 cm thick, 40.64 cm long, and 10.16 cm wide, were located directly beneath the muon funnel. They were arranged in to provide maximum probability of a vertical muon path with only a 10° entrance window. Each

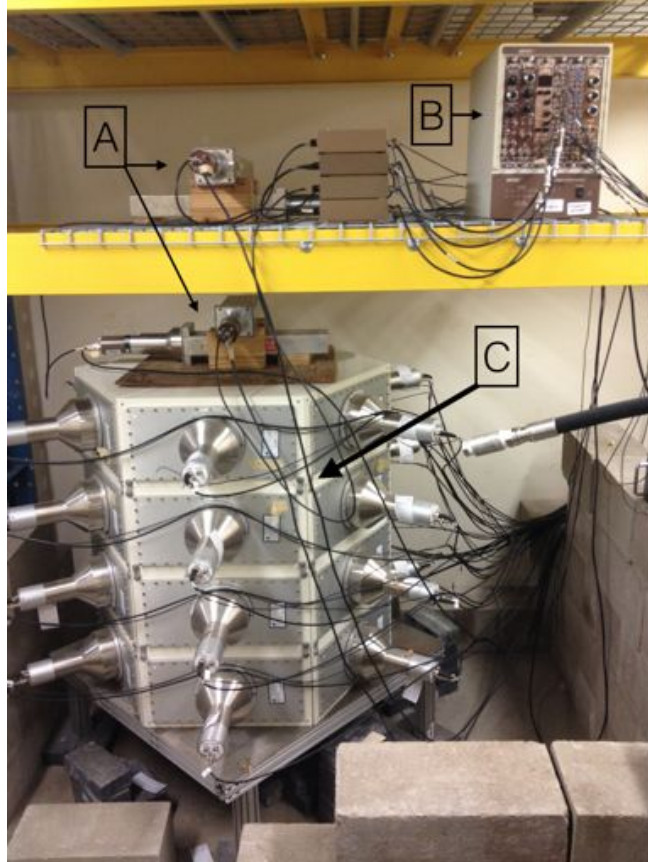


Figure 10. This illustration shows the A) NaI(Tl) scintillation detectors, B) logic coincidence trigger, and the C) neutron detector array used to detect cosmic muons in coincidence with their produced neutrons within the material to be examined. The material was placed at the center of the neutron detector array.

NaI(Tl) detector was powered using an Ortec 556 high voltage power supply at 1200 Volts. The output of each detector went directly into an Ortec 113 preamplifier with a 200 picofarad capacitance selected. The detector-preamplifier combinations were used primarily to determine a coincident muon event, and, as a secondary objective, to determine the energy spectrum of the incident muons. To accomplish both tasks simultaneously, the preamplifier output was split. The primary signal was passed on to an Ortec 935 quad constant fraction discriminator and then to an Ortec 4020 quad 4-input logic unit. The logic unit was set to output a signal only in the case where all four NaI(Tl) received a pulse simultaneously. In such a case, the output was used as the coincident trigger and was fed to the external trigger input for the CAEN V1724

and three CAEN V1720 digitizers with a CAEN V1718 controller. The secondary signal was fed directly into the input channels 0, 1, 2, and 3 of the CAEN 1724 board. This data was filtered and captured by the DPP-PHA pulse height analysis software provided by CAEN with settings seen in Appendix A. The output was saved using list mode and post processed through a Matlab script which can be seen in Appendix E. The muon detection portion of the experimental setup is illustrated in Figure 11.

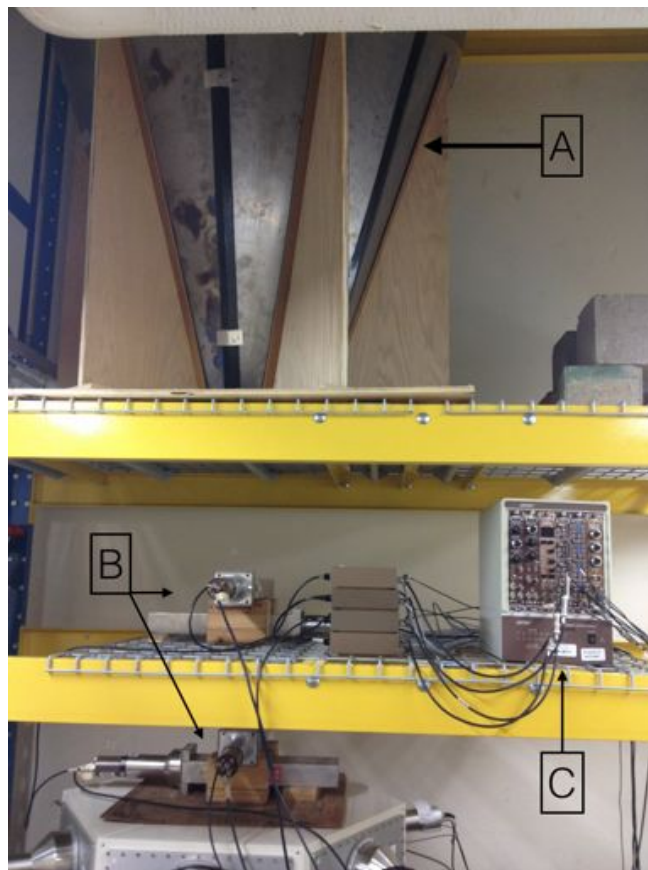


Figure 11. This illustration depicts the A) muon funnel, B) NaI(Tl) scintillation detectors, and C) logic coincidence trigger used to determine the initial muon entrance into the material.

Neutron Detection.

Beneath the NaI(Tl) scintillation detectors, an array of 24 EJ-309 liquid scintillation detectors with five inch photomultiplier tubes were arranged into four rings of six detectors apiece. One such ring can be seen in Figure 12, while the entire array can be seen in Figure 13. All the detectors were powered through a CAEN SY4527 crate with a 24 channel 3 kV power supply module. Each detector had an optimum applied voltage level given by the manufacturer, Eljen Technologies. These voltages are listed in Appendix C for reference. The detector outputs were passed to CAEN V1720 digitizers where the signals were recorded and PSD values were calculated using the DPP-PSD firmware provided by CAEN. The settings for the DPP-PSD firmware can be seen in Appendix B.

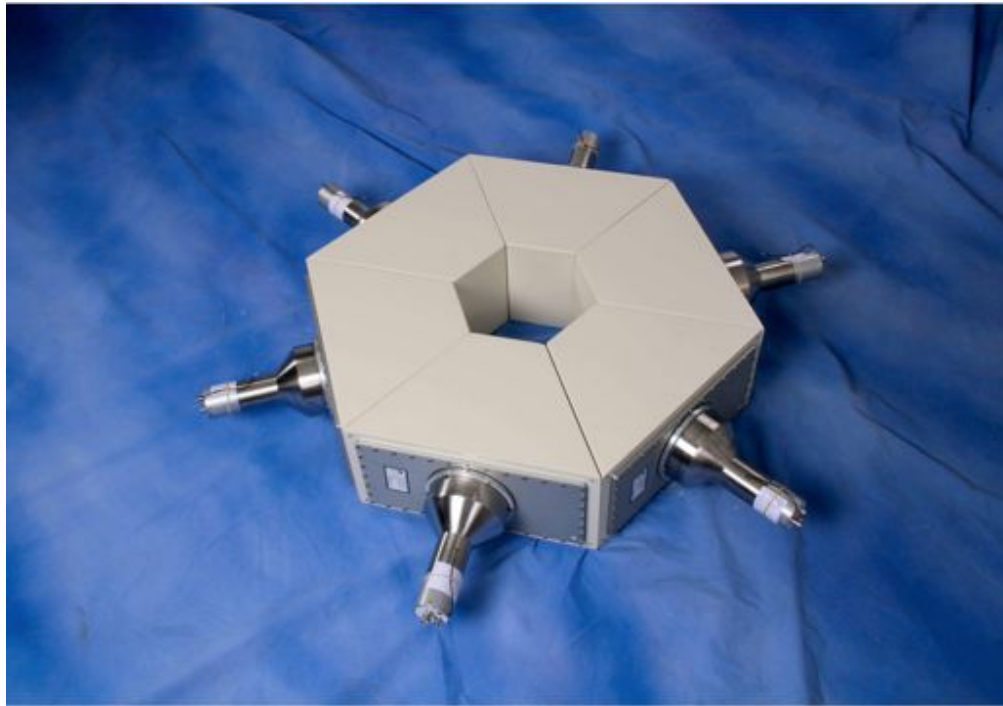


Figure 12. The EJ-309 neutron detectors were constructed to fit six per ring of the neutron array with enough room in the center to place material for inspection.

Previously a 77 mCi plutonium beryllium source had been utilized to examine the PSD values produced by the liquid scintillators used in this experiment. Figure

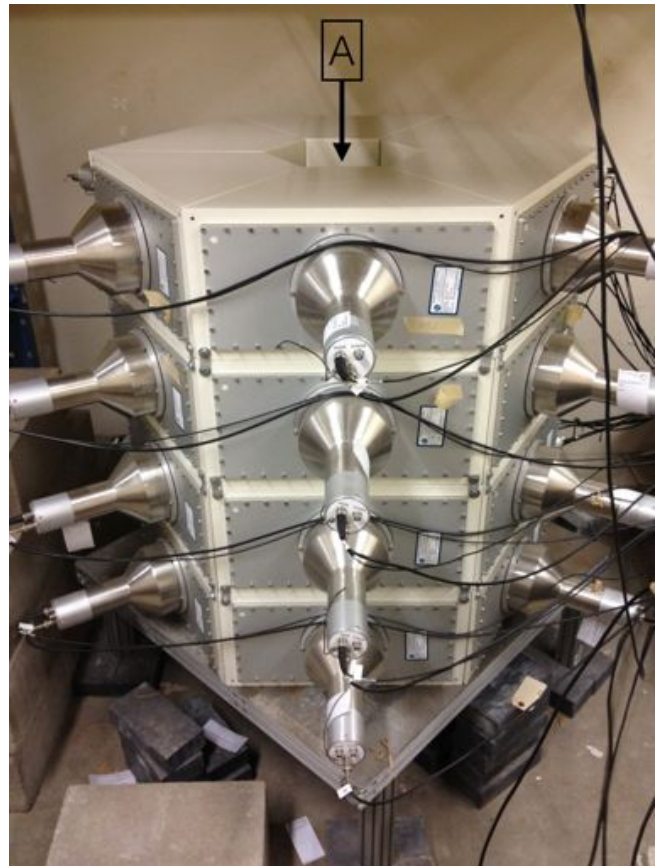


Figure 13. The neutron detector array is composed of 24 EJ-309 liquid scintillation detectors. This array provides nearly a 4π solid angle of detection capability when material is placed directly at the center of the array (A).

14 displays the acquired 2D histogram for both the gammas and neutrons that were detected by the liquid scintillators. A filter was applied to the PSD values in post processing to eliminate as many gamma events as possible by choosing cut lines at PSD values of 0.1 and 0.3 for the lower and upper limits respectively.

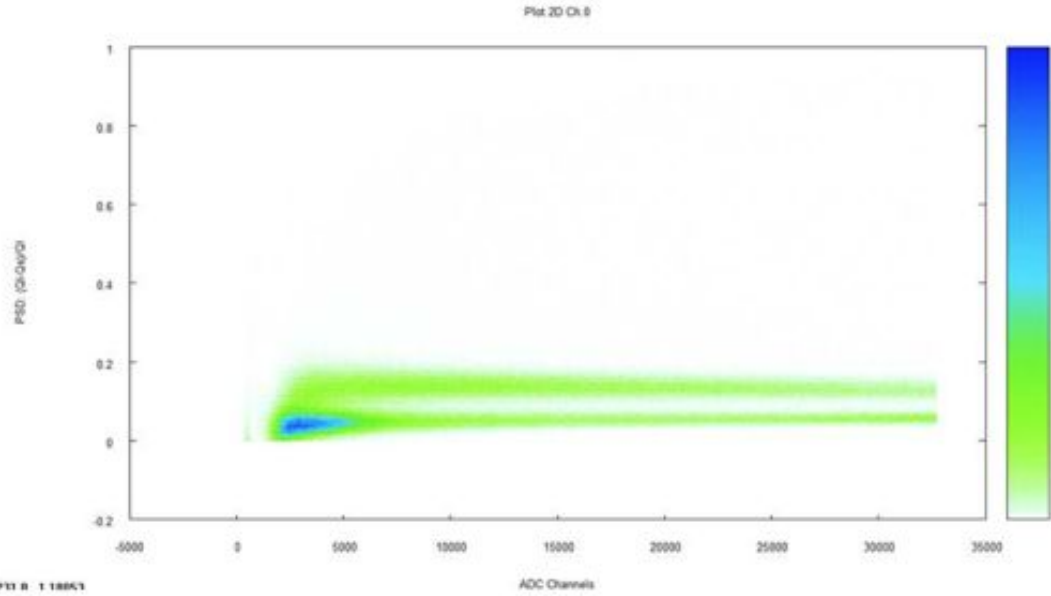


Figure 14. PSD 2D histogram used to determine neutron discrimination cut lines. The lower and upper cut lines were selected at PSD values of 0.1 and 0.3 respectively. Reproduced from Dr. Van Dyk's dissertation. [1]

Digitizer Synchronization.

An incompatibility in the clock synchronization between the two different CAEN digitizer boards, V1720 and V1724, prevented accurate correlation between the incident muon events and the neutrons that were produced. To solve this problem, one channel on each of the three CAEN V1720 digitizers was switched from one of the liquid scintillator detectors and replaced with an input signal from a Hewlett Packard 33120A function generator which can be seen in Figure 15. A 1 V, 10 MHz square pulse was continuously provided to each digitizer to ensure a recorded time stamp every time the external trigger was set off by an incident muon. In order to accomplish

this, three of the bottom neutron detectors were taken offline and their data was not gathered. Once the data had been gathered for each run, a Matlab script was used to correlate the timestamps for each neutron event to one incident muon. This script can be seen in Appendix E.



Figure 15. A function generator was used to ensure time stamps for every neutron detection were recorded with each muon event, since clock synchronization between the two different digitizer boards was not possible.

IV. Results and Analysis

4.1 Modeling Results

To examine the feasibility of using the phenomenon of μ IF as a detection method, the muon induced neutron production rates need to be determined for muon interactions with fissile materials. A simulation was performed to examine this characteristic utilizing the Monte Carlo simulation tool Geant4. This tool is produced by CERN to simulate the interaction and passage of high energy particles through matter and can be easily utilized to perform the necessary analysis.

Initial Modeling.

Initially, a 5 cm radius and 20 cm tall cylinder was simulated as the target material. A 4π spherical detector was created around the target material to detect and measure the emitted neutron energy spectra and counts. The entire volume, excluding the target material, was filled with air composed of 70% nitrogen and 30% oxygen. Muons were simulated as an isotropic point source located at the origin and centered within the target material allowing for maximum interaction. The entire geometry setup can be seen in Figure 16.

Five different target materials were used representing a wide range of atomic numbers and enrichment levels. These materials included enriched uranium, with an enrichment level of 90% ^{235}U and 10% ^{238}U , pure ^{238}U , lead, iron, and aluminum. Each of these materials was exposed to 100,000 muons at one of two different initial energies. The first trial was conducted at a muon source energy of 1 GeV. This energy was selected as it is on the order of the average energy of the cosmic muon flux at ground level after being moderated by 30 cm of concrete as seen in Figure 17. A second trial was conducted with a muon source energy of 100 MeV. This energy was

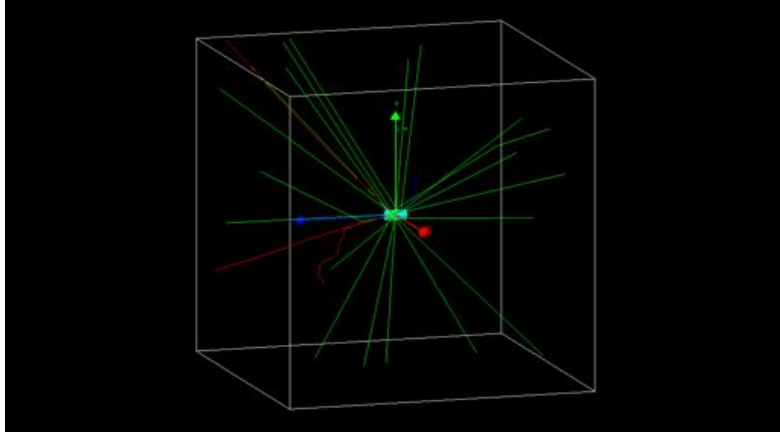


Figure 16. The geometry setup for the Geant4 simulation modeling muon induced neutrons. This figure does not display the 4π detector surrounding the target material. The green, red, and blue tracks represent neutral, negative, and positively charged particles created from the initial muon interactions.

selected as it is on the lower side of the cosmic muon spectrum, but has much higher neutron production rate within the target materials.

100 MeV Muon Source.

As can be seen from Figure 18, the neutron energy spectra from each of four materials have both quantitative and qualitative differences. As expected the enriched uranium target produced the most neutrons with the ^{238}U target following closely behind. However, both uranium targets produced 50% more neutrons than the lead target and a factor of 3 greater than the iron target. It should also be mentioned that although a trial run was conducted for each of the five materials, aluminum did not produce a statistically significant number of neutrons to be able to construct a spectrum.

1 GeV Muon Source.

As the energy of the muon source was increased to 1 GeV, the number of neutrons produced were reduced. In fact, although the increase in energy was only one order

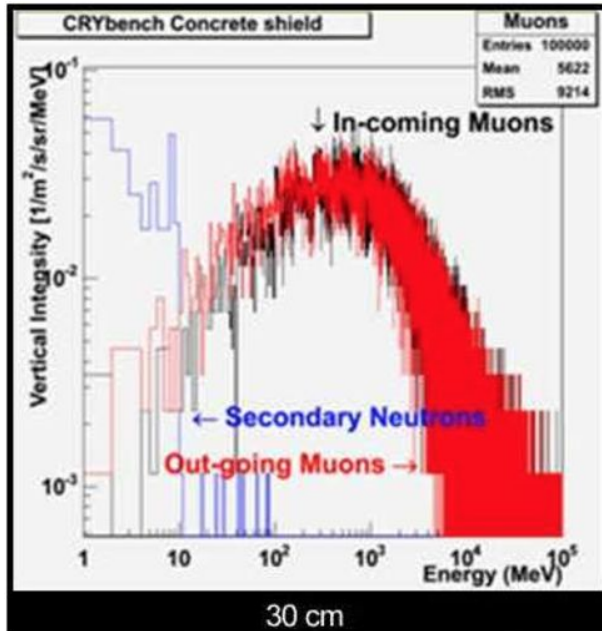


Figure 17. This plot displays the muon energy spectrum after being moderated by 30 cm of concrete, much like has been done in this experiment. Secondary neutrons are created through muon interactions with the concrete. The figure has been reproduced from work in the public domain by the Department of Energy. [27]

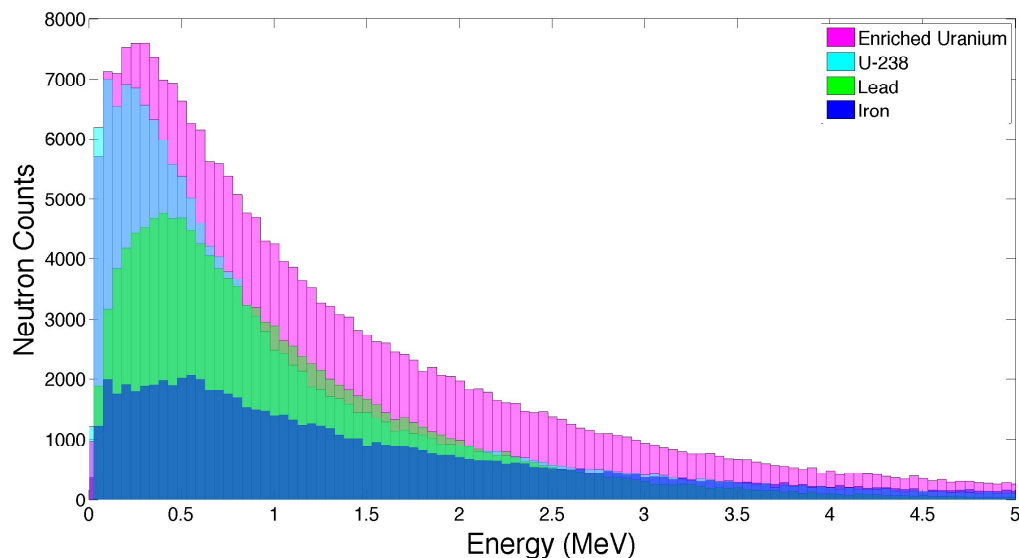


Figure 18. Muon induced fission neutron energy spectra from four different materials produced using 100 MeV muons. It should be noted that although aluminum was also simulated, the neutron production was negligible and no spectrum was produced.

of magnitude, the neutron count decreased two orders of magnitude in uranium and three orders of magnitude in lead and iron. In addition to the lack of counts, the spectra became much more sparse than their counterparts corresponding to the same material with the 100 MeV source but reducing or removing any noticeable features. These spectrums can be seen in Figure 19. Once again, the simulation ran all five materials. However, similar to the 100 MeV muon source, the aluminum target did not produce a single neutron and is therefore not displayed.

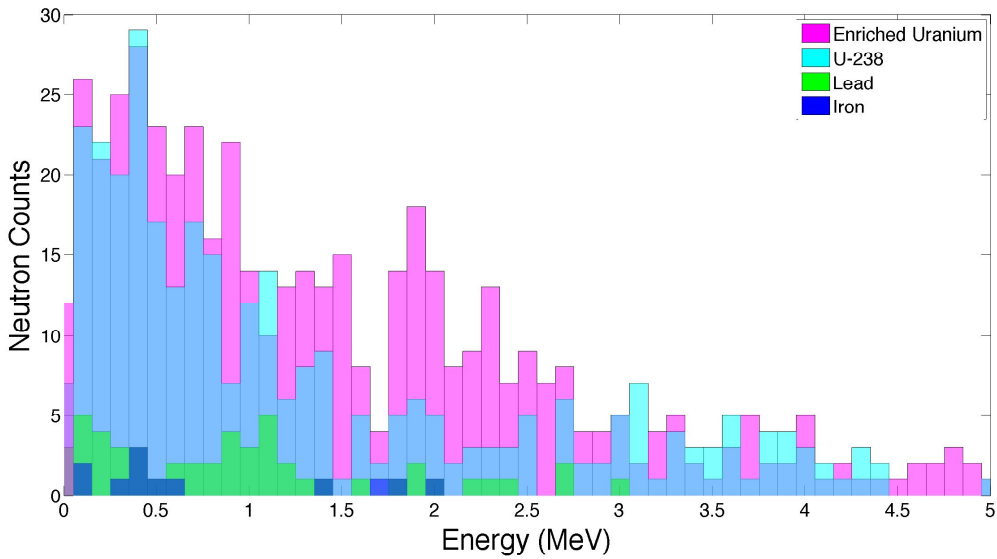


Figure 19. Muon induced fission neutron energy spectrums from four different materials produced using 1 GeV muons. It should be noted that although aluminum was also simulated, the neutron production was negligible and no spectrum was produced.

Neutron Yield per Muon.

When considering the detection capability and usefulness of muon induced fission, it is important to keep in mind that the neutrons produced from each fission event may act as a secondary signal to be acquired and analyzed. Each additional signal gathered has the potential to deliver a greater confidence of the presence of SNM. Table 1 shows the average number of neutrons produced for each muon simulated. As

expected, the enriched uranium produced the most neutrons while aluminum yielded the least.

Table 1. Average Neutron Yield per Muon For Initial Simulation

	100 MeV	1 GeV
Enriched Uranium	2.3 ± 0.1	0.1 ± 0.1
Depleted Uranium	1.5 ± 0.1	0.1 ± 0.1
Lead	1.3 ± 0.1	0.1 ± 0.1
Iron	0.8 ± 0.1	0.1 ± 0.1

Final Modeling.

After the initial modeling attempt, a more accurate simulation of the experiment was required. For this simulation, a block of material was created as the target and located at the center of the world volume. A 4π spherical detector with a 1 meter radius was created around the target material to detect the number of neutrons produced. The entire volume, excluding the target material, was filled with air composed of 70% nitrogen and 30% oxygen. Muons were created at a distance of 1.5 meters from the origin and given an initial velocity towards the target block. Upon interaction, only immediate daughter products of muon interactions were found and recorded, as well as any neutrons that passed through the detection sphere. In these scenarios, three materials were selected to be modeled, 90% enriched uranium, lead, and iron. Each material had a $20\text{ cm} \times 10\text{ cm}$ surface exposed to the incident muons, with the thicknesses varied. The lead and enriched uranium were 5 cm thick, while the iron and another lead simulation were conducted with a target block thickness of 15 cm. These thicknesses were selected as they corresponded to the available material on hand for the physical experiment. An example of the target material and its setup can be seen in Figure 20.

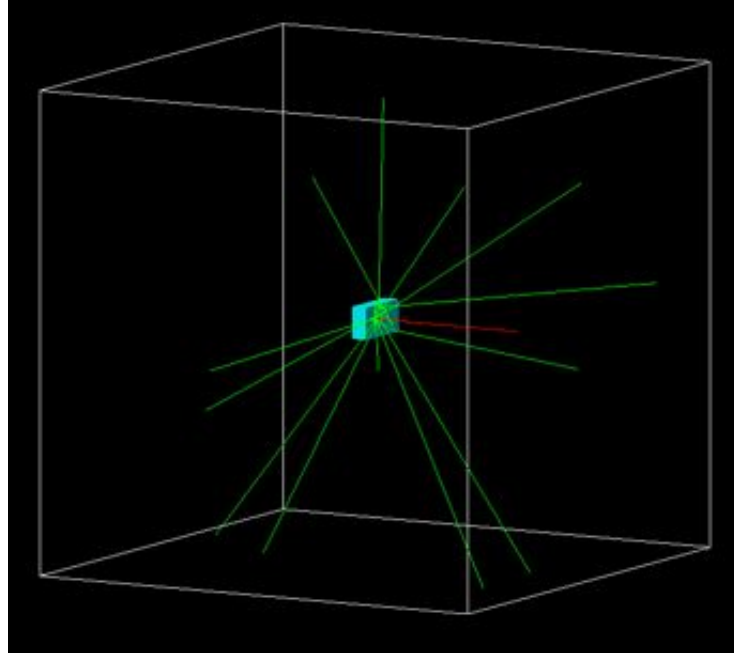


Figure 20. The geometry setup for a Geant4 simulation modeling muon induced neutrons in a 5 cm thick lead target. This figure does not display the 4π detector surrounding the target material. The green tracks represent neutral particles created from the initial muon interactions, while the red track is the incident muon path.

To gain a better understanding of the muon interactions at higher energies, two additional energy simulations were conducted. Initial muon energies of 100 MeV, 1 GeV, 10 GeV, and 100 GeV were selected and 100,000 muons were simulated for each energy on each material. The resulting neutron yields and their errors can be seen plotted in Figure 21.

As can be seen in Figure 21, the 100 MeV incident muons produced several orders of magnitude more average number of neutrons than those at higher energies. However, there is an increase in neutron production with an increase in incident muon energy greater than 1 GeV. Inspection into the documentation on the cross sections utilized by Geant4 revealed that little is known about the cross sections in the region of low muon energy below approximately 1 GeV for neutron production. Inelastic interactions between muons and nuclei gains importance at energies above 10 GeV, while below this threshold minimal neutron production occurs via this method. How-

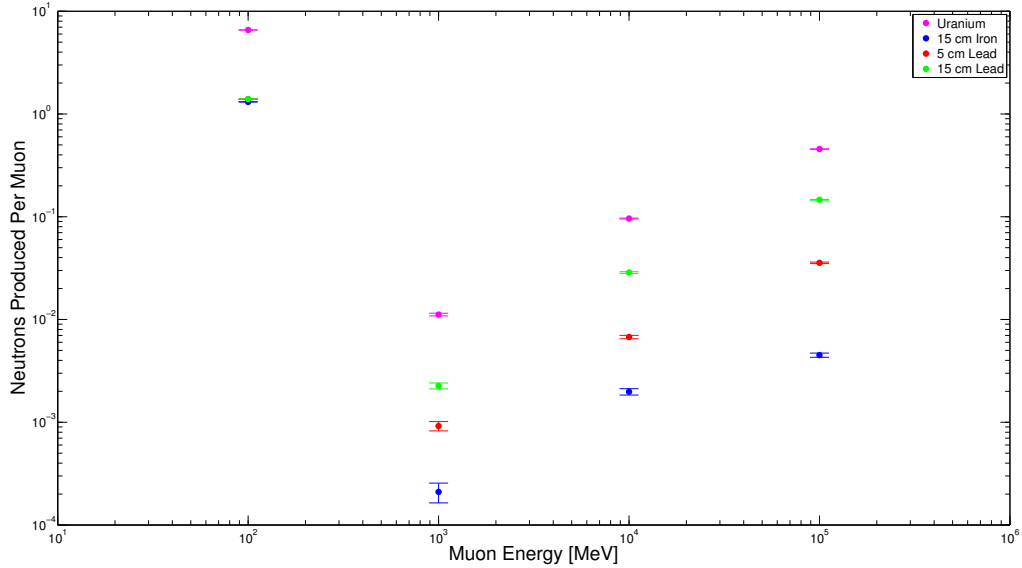


Figure 21. The dependence of average neutron yield on muon energy for four different material and geometry configurations.

ever, in the event that the muon can be thermalized, the capture process dominates within the simulations though the Geant4 process name of muMinusCaptureAtRest, but no cross sections are listed. This is indeed in line with the neutron yields produced within this simulation. Total neutron yields of the final simulation can be seen in Table 2.

Table 2. Average Neutron Yield per Muon For Final Simulation

	100 MeV	1 GeV	10 GeV	100 GeV
5 cm Uranium	6.6 ± 0.1	0.1 ± 0.1	0.1 ± 0.1	0.1 ± 0.1
5 cm Lead	1.4 ± 0.1	0.1 ± 0.1	0.1 ± 0.1	0.1 ± 0.1
15 cm Lead	1.4 ± 0.1	0.1 ± 0.1	0.1 ± 0.1	0.1 ± 0.1
15 cm Iron	1.3 ± 0.1	0.1 ± 0.1	0.1 ± 0.1	0.1 ± 0.1

In terms of detection capabilities, the neutron yield at the lower muon energies may be able to be utilized as a secondary detection method. However, when considering

atmospheric muon energies, simulations suggest most muons will not contribute to the generation of this signal unless they are previously moderated to lower energies. If it could be arranged for some type of moderating material to be placed between the target and the source, an increase in neutron production may be seen.

4.2 Experimental Results

To perform the experiment, blocks of iron and lead were placed at the center of the array of neutron detectors. These materials were chosen because of their availability and varied atomic number. Each material had an exposed area of $20\text{ cm} \times 10\text{ cm}$ exposed to the incident muons, but the thickness was varied. The iron block had a thickness of 15 cm while two blocks of lead were used with thicknesses of 5 cm and 15 cm. Every trial was performed for a duration of seven days with an additional seven day measurement of natural background neutron levels.

Muon Energy Determination.

In order to properly classify an event as muon-induced, the muon event was detected in coincidence by four NaI(Tl) scintillation detectors. These detectors captured pulse height information which was converted to energy through a calibration method which is detailed in Appendix D. The NaI(Tl) detectors were calibrated using known gamma sources of Cs-137 and Co-60. In addition to the low energy gamma sources, a higher energy point was used with the most likely energy deposited in the detectors corresponding to the minimum ionizing potential for the NaI(Tl) detectors found using Equation 6 to be 24.297 MeV.

Once this calibration was applied, pulse heights could be converted to energy deposited within the NaI(Tl) detectors. The energy deposited was then filtered to remove any energy deposition events not consistent with that anticipated by the

Bethe-Block equation for a muon event. The minimum threshold was chosen to be the minimum ionizing potential of 24.297 MeV, while the maximum threshold was chosen to be the expected energy deposition of a 5 GeV muon of 31.75 MeV. Each threshold was also modified to compensate for a detector resolution of 12% by setting the threshold value at 3σ below and above the stated values, respectively.

After threshold values had been applied for each muon event, a muon energy was varied from 140 - 5000 MeV in 1 MeV increments for a muon event incident upon the first NaI(Tl) detector. Each of these incident energy values was then used to determine the theoretical energy deposition in each of the four NaI(Tl) detectors using Equation 6. The theoretical values were then compared to the measured values using Pearson's χ^2 test statistic calculated using Equation 11.

$$\chi^2 = \sum_{i=1}^4 \frac{(dE_{i,BB} - dE_{i,measured})^2}{dE_{i,BB}} \quad (11)$$

where $dE_{i,BB}$ is the theoretically predicted energy deposited in each of the NaI(Tl) detectors and $dE_{i,measured}$ is the experimentally measured energy deposited.

The initial muon energy that resulted in the lowest χ^2 test statistic was the most likely energy of the muon incident upon the system. The theoretical energy of the muon leaving the last NaI(Tl) detector was then calculated and used as the muon energy incident upon the target. The final muon energy distribution can be seen in Figure 22. Previous experiments utilizing the same experimental setup have found the mode and mean of the distribution to be 550 MeV and 926 MeV respectively [1]. However, this series of experiments found the mode and mean of the distribution to be approximately 180 MeV and 520 MeV respectively. The discrepancy likely rises from a change in the operating voltage of the NaI(Tl) detectors and differences in calibration methods.

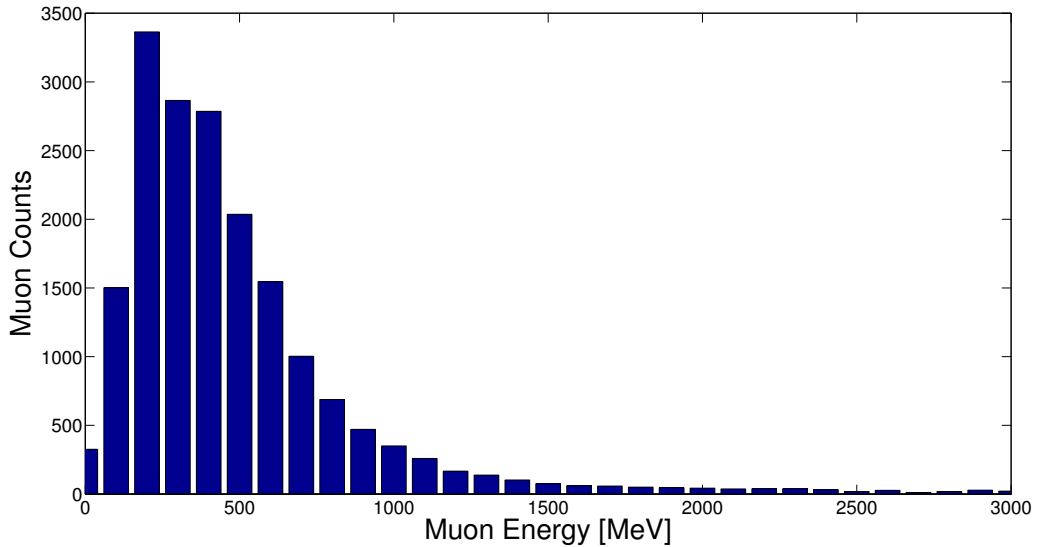


Figure 22. This figure displays the incident muon energy distribution after passing through the muon funnel and all four NaI(Tl) detectors. The slight spike located at approximately 200 MeV corresponds to the location of the minimum ionizing potential in the Bethe-Block equation.

Neutron Yield Analysis.

The number of neutrons produced for each muon event were recorded and are displayed in Figure 23.

As was expected, when no material was present the majority of incident muons were detected in coincidence with zero neutrons. The number of muons producing one neutron decreased by an order of magnitude, and again by another order of magnitude when two neutrons were produced. However, an interesting feature arose when the neutron counts were observed with material present. In all but one case, the number of muon events that produced zero neutrons was less than the amount that produced one neutron. This suggests that a majority of the muons that are incident upon the material, interact in such a way as to produce at least one neutron and is supported by the average neutron calculation based upon the simulation results. This assumption is supported further by examining the neutron counts once the background neutron levels have been removed as seen in Figure 24. In such a case, a change in the

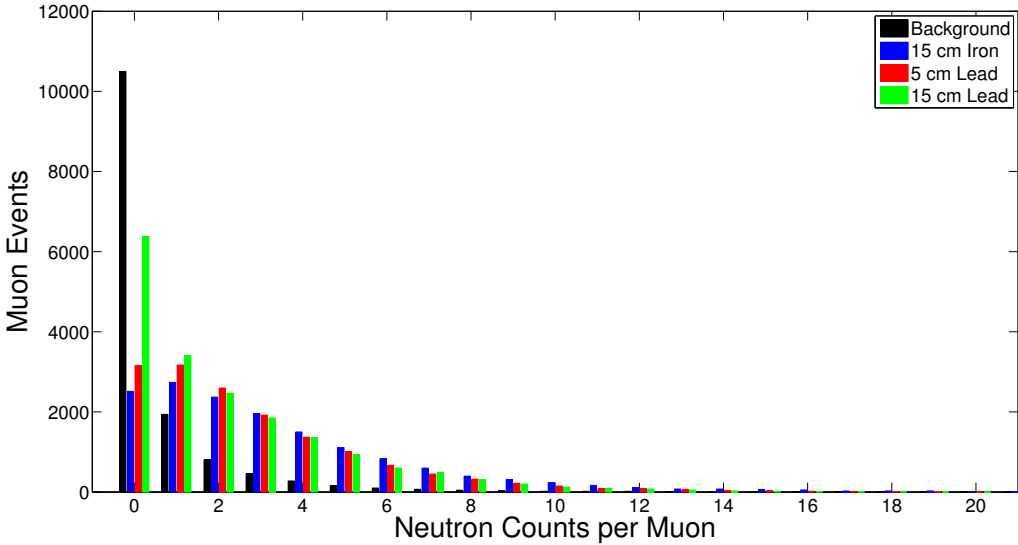


Figure 23. This figure displays the frequency of occurrence for each neutron yield over the course of the seven day experiment.

maximum neutrons produced is seen as an increase from one neutron being produced for an incident muon to two produced neutrons.

In order to directly compare the neutron yields from the different materials and geometries, the muon counts were scaled to produce the probability distribution displayed in Figure 25. These calculated probability distributions display the likelihood that a specific number of neutrons will be detected above the background levels based upon the data gathered over the seven day period for each sample. A two sample t-test was performed comparing each data set to the other two, and the null hypothesis of $\mu_1 = \mu_2$ could not be rejected in any case with the lowest p-value being 86% suggesting that all data sets are likely correlated.

Mean neutron yield per detected muon was calculated for the experimental results in the same manner as the simulated results, using total muons and total neutrons detected. These results displayed in Table 3. Immediately an anomaly arose when inspecting the average neutron yield per muon, as the 15 cm block of lead produced the lowest average neutron yield. However, for a period of time the power to the

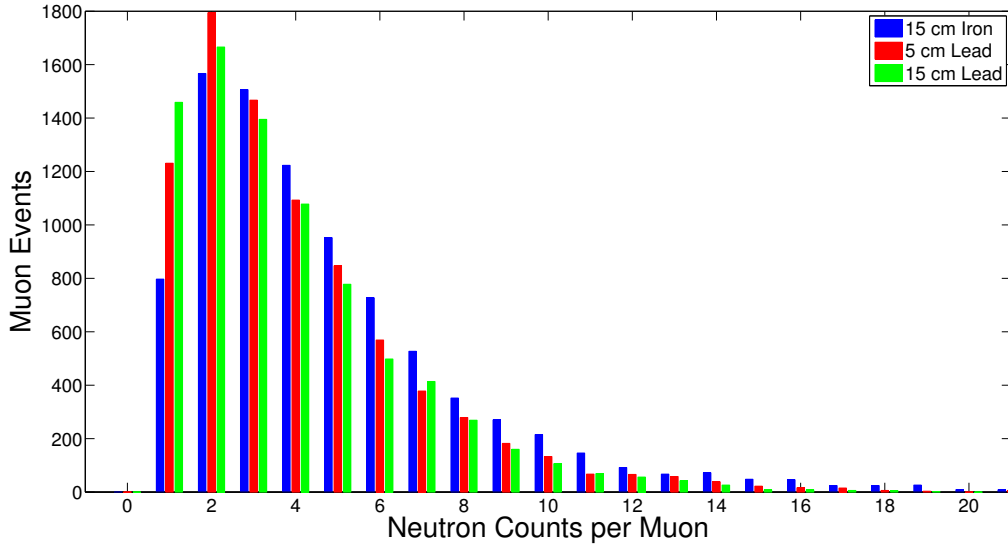


Figure 24. This figure displays the frequency of occurrence for each neutron yield after background levels were removed.

neutron detectors was temporarily shut off while power to the muon coincidence unit remained functional. The result of this power fluctuation resulted in a higher number of muons passing through the material than the neutron data accounts for. This difference also explains the uniqueness of the 15 cm lead data in Figure 23 having a higher muon count at a neutron yield of zero than of one.

Table 3. Mean neutron yields per muon after 7 days of exposure

Material	Total	Above Background	100 MeV	1 GeV
5 cm Lead	2.8 ± 0.1	4.0 ± 0.1	2.1 ± 0.1	2.1 ± 0.3
15 cm Lead	2.2 ± 0.1	3.8 ± 0.1	1.6 ± 0.1	1.1 ± 0.2
15 cm Iron	3.4 ± 0.1	4.8 ± 0.1	3.0 ± 0.2	2.1 ± 0.3

Additionally, the mean values for the number of neutrons produced above the background levels were calculated and can also be found in Table 3.

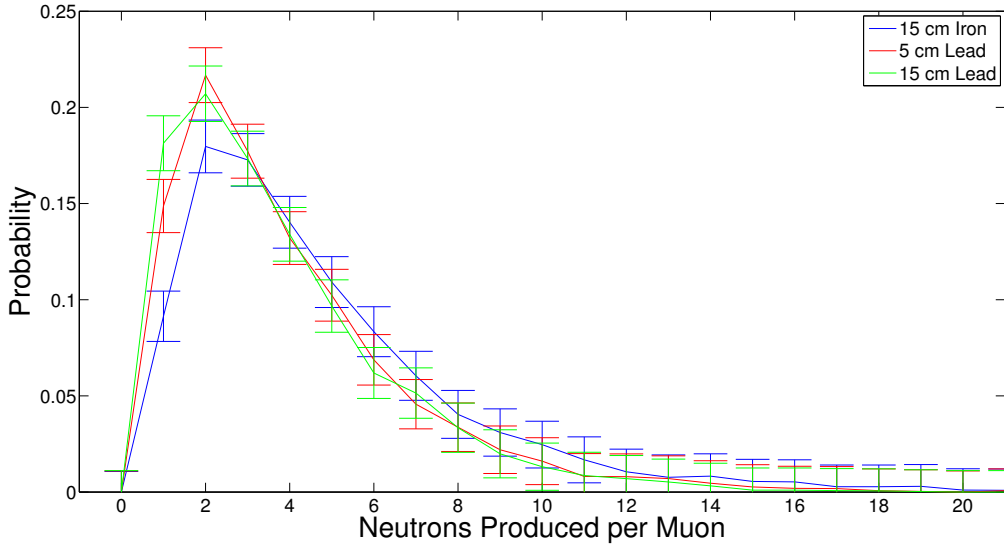


Figure 25. The probability distribution for an incident muon to produce a given neutron count above background levels.

Energy Dependent Neutron Yield.

To further compare the neutron output found experimentally, the neutron yields were plotted against incident muon energy, and can be seen in Figure 26. In these plots, each point represents one muon event. A qualitative increase in neutron production can be seen visually between the background measurement and the addition of any material.

To further analyze this information, the muon events were binned by energy in 100 MeV increments and their average neutron yields calculated. At lower energies a more consistent neutron yield was produced, but the noise increased with incident muon energy. To gain a better understanding of this phenomena, the neutron yield was plotted with the corresponding error in each point in Figure 27. The increased noise at higher incident muon energies is to be expected as the muon energy distribution was primarily below 1000 MeV leading to very poor counting statistics in the higher energy region.

Another two sample t-test was conducted to compare each of the materials average

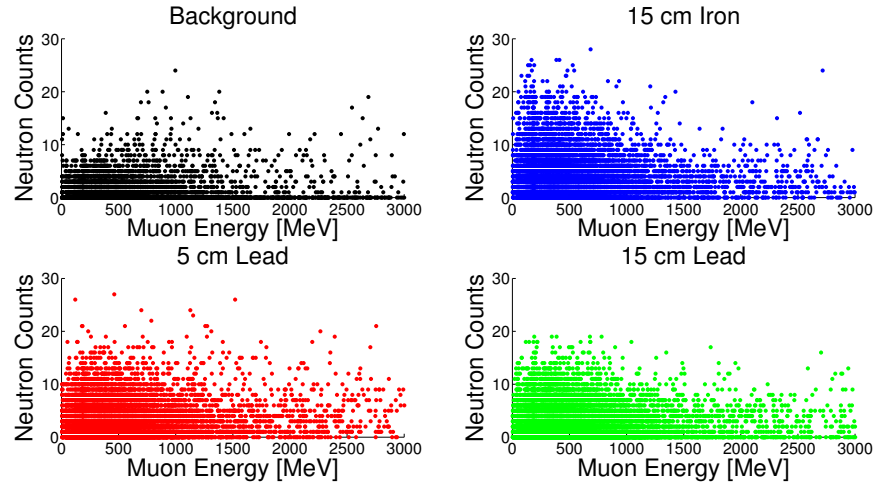


Figure 26. This figure displays the number of neutrons produced by and energy of each muon incident on the system. Visual inspection reveals that neutron counts are above background level, but more quantitative analysis must be done to distinguish between materials.

neutron output to the other three sets of data. In each case the null hypothesis of $\mu_1 = \mu_2$ could be rejected with a 95% probability. This result suggests that the muon energy dependent neutron yields of each material were not equivalent. It is predicted that a poor PSD filter has been applied to the data. This would mean that gamma events created within the target material are being counted as neutrons when detected by the liquid scintillation detectors, artificially increasing counts. In such a case, additional gamma events would reach the detector when produced in the iron target that would be attenuated when created within the lead target.

Finally, the incident muon energy spectra were examined based upon the neutron yield of that particular event. As seen in Figure 28, the spectra shape are similar to the incident muon energy spectrum seen in Figure 22. Also important to note are the relative heights of each material's spectra. With a neutron yield of zero, one, or two neutrons created, the order is as expected. However, when three or more neutrons are produced, the peaks of the spectra begin to overlap and become indistinguishable from one another. These features agree with the previous findings seen in Figure

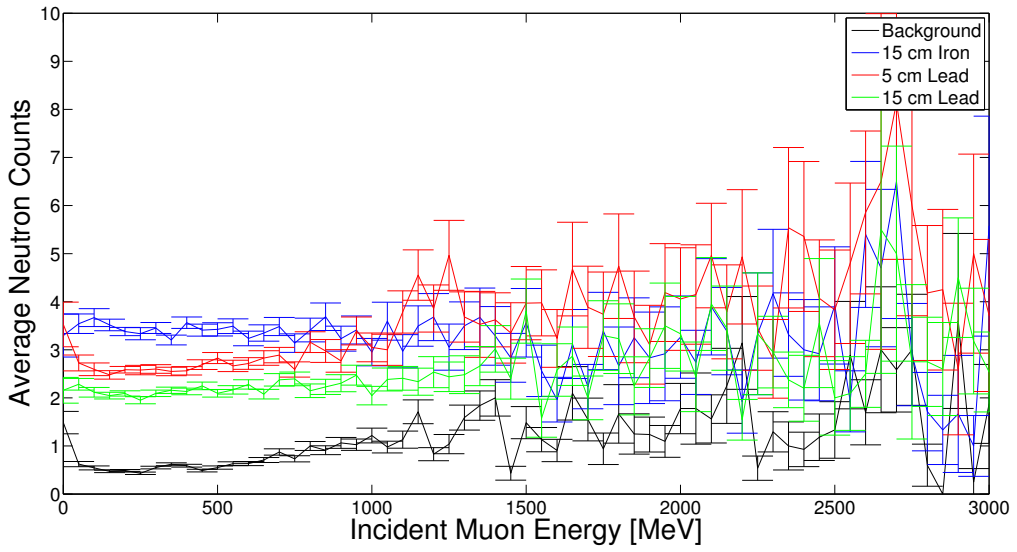


Figure 27. This plot displays the average neutrons produced for a muon with a given energy incident upon the system.

25 with both lead samples yielding more events with a neutron yield of one and two neutrons, but the overlap between lead and iron begins to occur with a three detected neutrons.

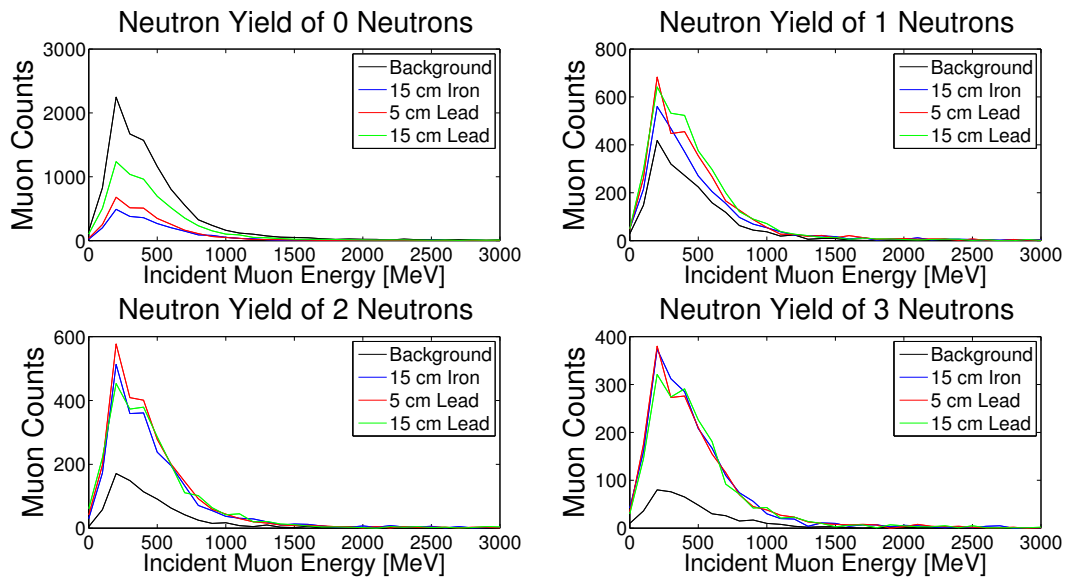


Figure 28. This figure displays the muon energy spectra for various neutron yields. As expected it follows the shape of the incident muon energy distribution in all cases. Above a neutron yield of three neutrons the muon counts continue to decrease, but the general shape of the spectrum remains the same.

V. Conclusions

5.1 Research Summary

As the need for better imaging and noninvasive interrogation techniques rises, the applicability of muon imaging techniques grows. In these scenarios, cosmic and atmospheric muons can offer superior penetrating capabilities and can be utilized to determine the contents of a sealed container such as a shipping container or a nuclear weapon. However, due to the requirement of a detector on both sides of the target material, the feasibility of utilizing these techniques for real world applications diminishes. Secondary signals may help to provide an alternate means of utilizing muon imaging in telescopic mode. Initial findings suggest neutrons produced by muon induced fission may be able to provide one such secondary signal.

Initial simulations of two different muon energies, 100 MeV and 1 GeV, were performed on five different materials of various atomic numbers. Neutron energy spectrums were gathered and analyzed for each of the five materials. The neutron yields per muon were calculated and found to range from between 2.3 ± 0.1 for enriched uranium down to negligible amounts for aluminum when exposed to the 100 MeV source. As the energy of the muons was increased to 1 GeV, the neutron yields shrank to negligible levels. These simulations also suggested that there is little difference in neutron yield produced in non-fissile material while the neutrons produced in an enriched uranium block was greater by a factor of five.

Experimental results differed from these findings. A probability distribution was constructed from the neutron yields of each incident muon. The various probability distributions produced by both the iron and lead, as well as the two different thicknesses of lead were nearly identical. Statistical T-tests were conducted to compare the various distributions to one another. In no case were the results conclusive and

able to reject the null of $\mu_1 = \mu_2$ suggesting minimal difference in the distributions. The average neutron yield was also calculated and found to be 3.4 ± 0.1 for a 15 cm thick block of iron, 2.8 ± 0.1 for a 5 cm thick block of lead, and 2.2 ± 0.1 for a 15 cm thick block of lead.

The energy distribution was found for a muon incident upon the system and average neutron yields were calculated for each 100 MeV region. The average neutron yields were plotted against incident muon energy and statistical T-tests were conducted comparing the various materials' distributions to one another. In every case, the null hypothesis of $\mu_1 = \mu_2$ could be rejected with a 95% probability suggesting that the distributions were statistically different. Additionally, incident muon energy spectra were examined for each neutron yield output and differences began to diminish above three detected neutrons.

From these findings, muon imaging operated in telescopic mode may be able to detect SNM within an enclosed container by observing the neutron output. Simulations indicate that highly enriched uranium will provide a significant increase in neutron output when compared to other materials such as lead and iron. In addition, if incident muon energy can be determined other materials may be able to be distinguished by examining the muon energy dependent neutron output.

5.2 Future Work

Since muon imaging holds such promise for accurate detection of SNM in both portal inspection points and international treaty verification, further work in this area is highly recommended. As a follow on to this experiment, a more accurate method of muon energy determination would benefit the accuracy of any findings. Another topic of study which would be helpful in the determination of neutron output, would be to examine in further detail the PSD values for neutron and gamma events in each liquid

scintillator as well as the PSD value of a muon within the same detectors used in this experiment. It is possible that atmospheric muons may be able to impart a similar PSD value as the neutrons increasing their count rate and thus yield. Finally, the most important experiment that must be performed is the analysis of muon induced neutron output in fissionable elements. While simulations do suggest neutron production at elevated levels, experimental confirmation is needed.

Appendix A. PHA Software Settings

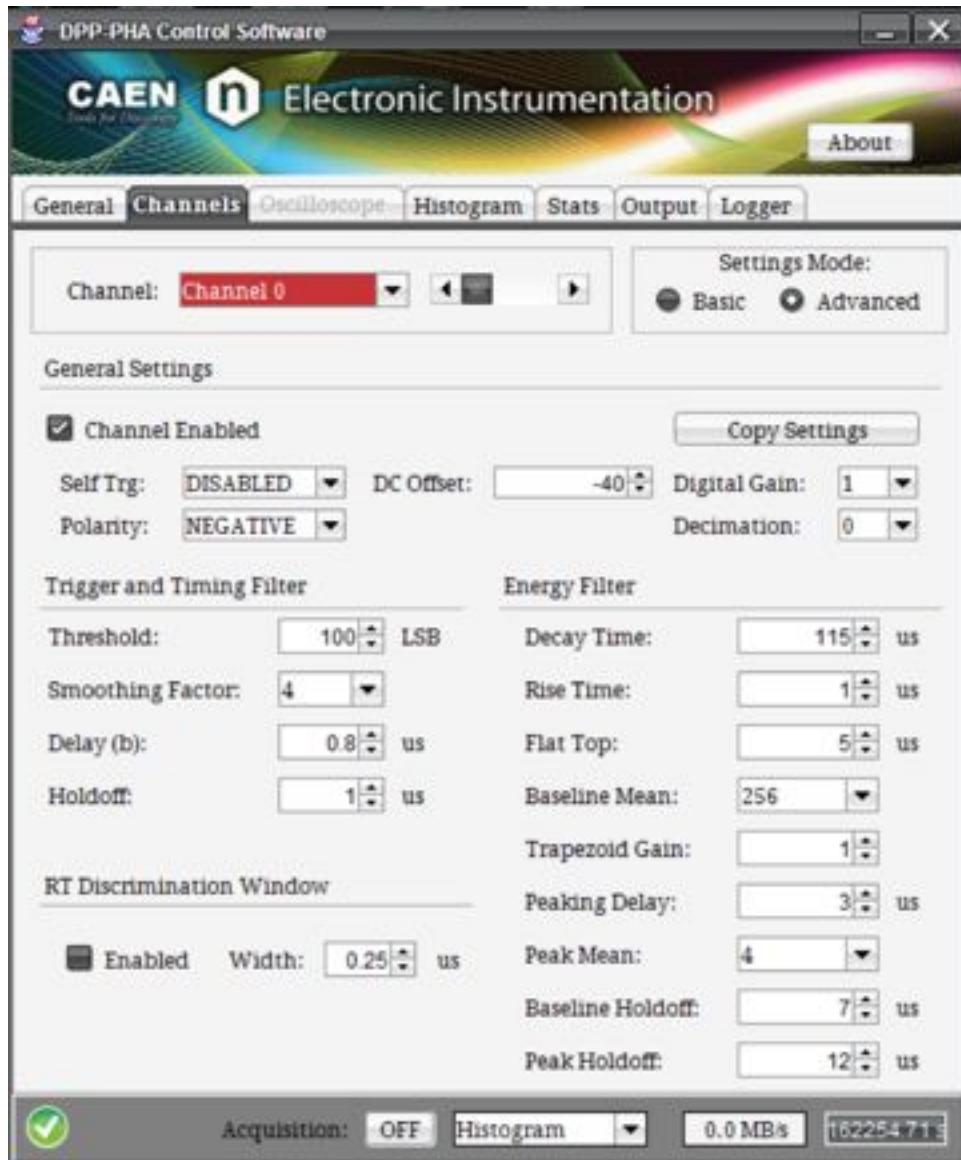


Figure 29. Computer software settings for pulse height analysis of the NaI(Tl) detectors.

Appendix B. PSD Software Settings

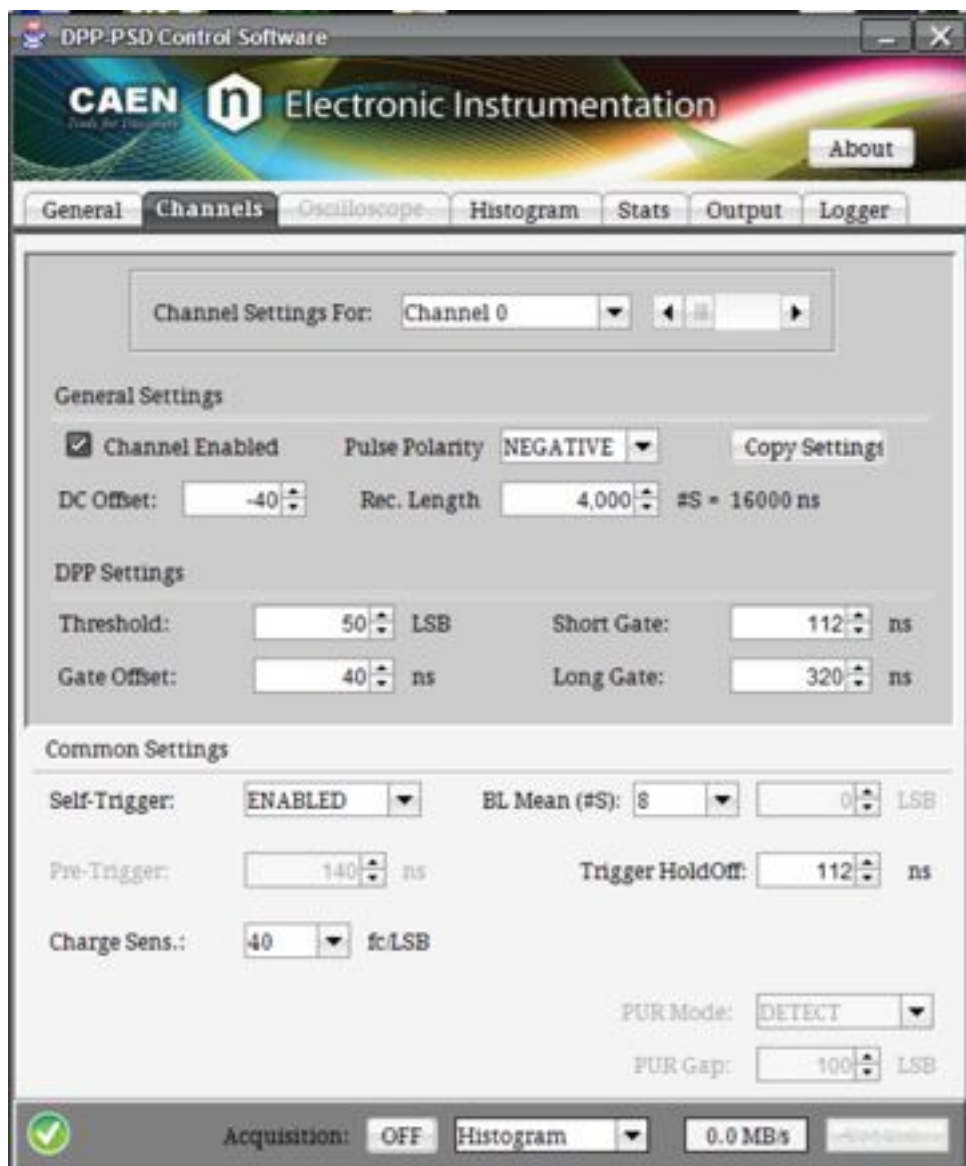


Figure 30. Computer software settings for pulse shape discrimination and neutron detection.

Appendix C. Neutron Detector Voltages

Table 4. Voltage settings for the various liquid scintillation neutron detectors.

Detector Number	Serial Number	High Voltage [V]
1.1	4587-01-21	1425
1.2	4587-01-19	1650
1.3	4587-01-22	1400
1.4	4587-01-23	1450
1.5	4587-01-14	1225
1.6	4587-01-13	1600
2.1	4587-01-05	1300
2.2	4587-01-10	1500
2.3	4587-01-11	1250
2.4	4587-01-02	1300
2.5	4587-01-06	1400
2.6	4587-01-24	1375
3.1	4587-01-04	1500
3.2	4587-01-18	1850
3.3	4587-01-17	1350
3.4	4587-01-20	1325
3.5	4587-01-16	1425
3.6	4587-01-12	1400
4.1	4587-01-08	1325
4.2	4587-01-09	1425
4.3	4587-01-07	1250
4.4	4587-01-15	1425
4.5	4587-01-01	1400
4.6	4587-01-03	1325

Appendix D. NaI(Tl) Detector Calibration

To properly calibrate the NaI(Tl) scintillation detectors two gamma sources were selected to provide known energy depositions within the detectors. A Cs-137 and a Co-60 source were selected from the available resources and provided three well known gamma energies of 662 keV, 1173 keV, and 1333 keV. The two sources were exposed to the NaI(Tl) detectors and spectra were gathered. Each of these spectra were then analyzed and the observed peak values were recorded. Because muon energy deposition primarily occurs at much higher energies than can be deposited by gamma sources, an additional point of higher energy must be used minimize extrapolation error.

To more accurately predict the energy deposition at these higher energies, the minimum ionizing potential can utilized. The most probable muon energy deposition corresponds to the minimum ionizing potential of 22.297 MeV in the NaI(Tl) detectors according to the Bethe-Block equation, Equation 6. Upon completion of an experimental run, the pulse height spectra were plotted for each of the NaI(Tl) detectors and can be seen in Figure 31. The maximum value of these peaks were determined to represent the minimum ionizing potential energy as has been done in previous experiments [1].

Once the pulse height channels were gathered from the minimum ionizing potential peak and the known gamma sources, they were plotted against the known energies.

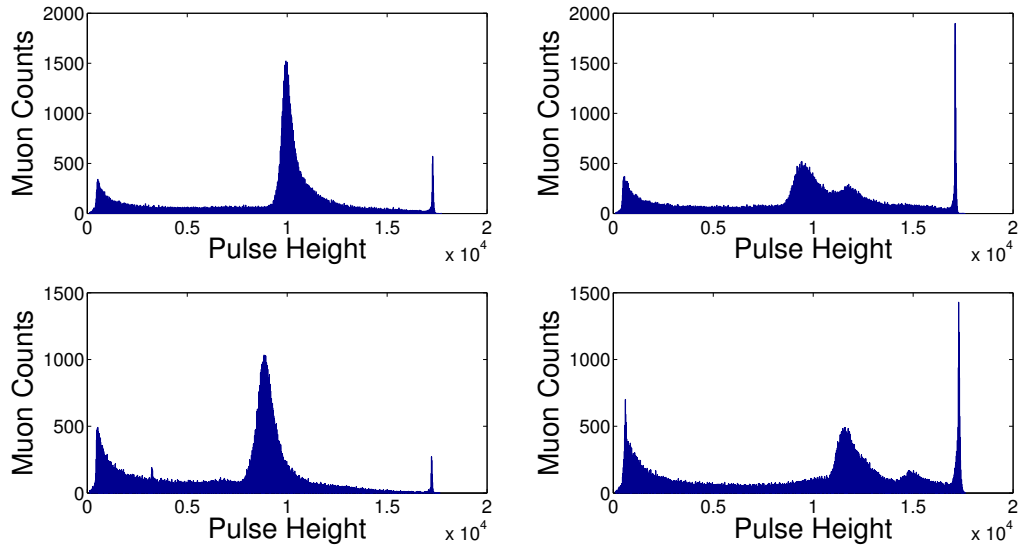


Figure 31. The peak value of the middle peak in the pulse height distributions were determined to be the minimum ionizing potential according to the Bethe-Block equation for NaI(Tl) with an energy of 24.297 MeV.

The calibration equations were calculated to be

$$\text{Detector1} : y = 400x + 220$$

$$\text{Detector2} : y = 380x + 170$$

$$\text{Detector3} : y = 360x + 100$$

$$\text{Detector4} : y = 450x + 670$$

and can be seen in Figure 32.

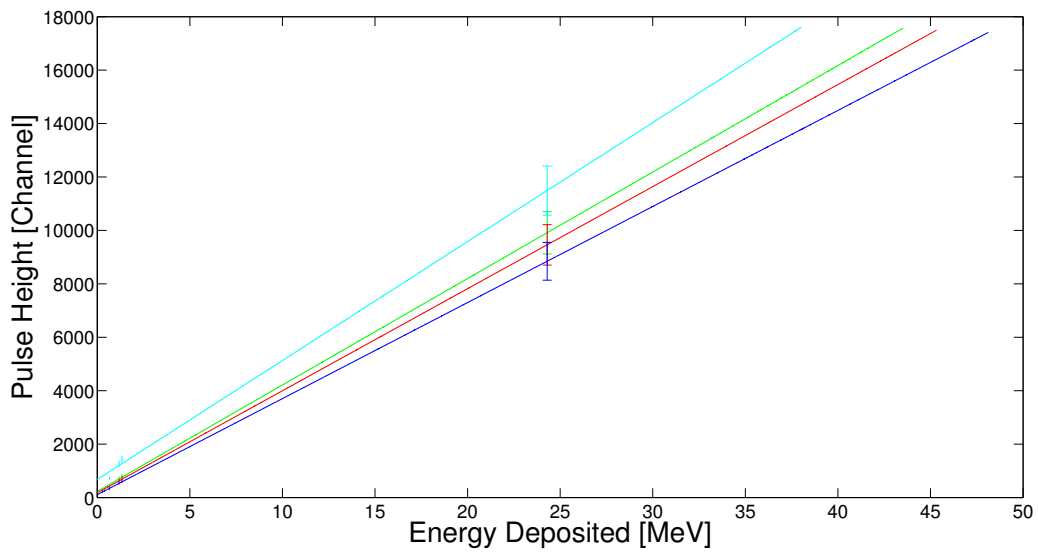


Figure 32. NaI(Tl) calibration curves for each of the four NaI(Tl) detectors. The calibration points with the associated error can be seen as well at 0.662 MeV, 1.173 MeV, 1.333 MeV, and 24.297 MeV.

Appendix E. Matlab Code

```
%%%%%%%%%%%%%%%%
%IMPORT Data
%%%%%%%%%%%%%%%
%Data import code for muon fission experiment
%Written by Lt Logan Brandt
%20 November 2014

clear;
clc;

%%%%%%%%%%%%%%
% Initialize Variables %
%%%%%%%%%%%%%%

NaI_channels = 4;
neutron_channels = 8;

Fe_runs = 6;
Pb1_runs = 3;
Background_runs = 2;
Pb3_runs = 5;

%
%%%%%%%%%%%%%%%
% IMPORTANT: Run each section individually and save the workspace as
```

```

% *type_of_material* Data.mat. This file type is a required input for
the
% analysis code.

%
%%%%%%%%%%%%%%%
%%%
%%%
%%% Import Iron Fission Data %%
%%%
%%% NaI channels
for i = 1: NaI_channels
    NaI = [];
    for j = 3:Fe_runs
        hold_file = load(['~/Users/LJBrandt/Documents/ThesisData/Fe/
Fe_PHA_00',...
        num2str(j) '_ls_' num2str(i-1) '.dat']);
        NaI = cat(1, NaI, hold_file);
    end
    NaI_Data{i} = NaI;
end

%%% neutron channels
for i = 0: neutron_channels-1
    PSD0 = [];
    PSD1 = [];
    PSD2 = [];
    for j = 3: Fe_runs

```

```

hold_file0 = load(['/Users/LJBrandt/Documents/ThesisData/Fe/
Fe_PSD0_00'...
num2str(j) '_ls_' num2str(i) '.dat']);

hold_file1 = load(['/Users/LJBrandt/Documents/ThesisData/Fe/
Fe_PSD1_00'...
num2str(j) '_ls_' num2str(i) '.dat']);

hold_file2 = load(['/Users/LJBrandt/Documents/ThesisData/Fe/
Fe_PSD2_00'...
num2str(j) '_ls_' num2str(i) '.dat']);

PSD0 = cat(1, PSD0, hold_file0);
PSD1 = cat(1, PSD1, hold_file1);
PSD2 = cat(1, PSD2, hold_file2);

end

PSD0_Data{i+1} = PSD0;
PSD1_Data{i+1} = PSD1;
PSD2_Data{i+1} = PSD2;

end

clear Background_runs Fe_runs hold_file hold_file0 hold_file1 hold_file2
...
i j NaI NaI_channels neutron_channels Pb1_runs Pb3_runs PSD0 PSD1
PSD2
%%
%%%%%%%%%%%%%
% Import 1 Block Lead Fission Data %
%%%%%%%%%%%%%

```

```

for i = 1: NaI_channels
    NaI = [];
    for j = 1: Pb1_runs

        hold_file = load(['/Users/LJBrandt/Documents/ThesisData/Pb1/
            Pb1_PHA_00'...
            num2str(j) '_ls_' num2str(i-1) '.dat']);
        NaI = cat(1, NaI, hold_file);

    end
    NaI_Data{i} = NaI;
end

for i = 0: neutron_channels-1

    PSD0 = [];
    PSD1 = [];
    PSD2 = [];
    for j = 1: Pb1_runs

        hold_file0 = load(['/Users/LJBrandt/Documents/ThesisData/Pb1/
            Pb1_PSD0_00'...
            num2str(j) '_ls_' num2str(i) '.dat']);
        hold_file1 = load(['/Users/LJBrandt/Documents/ThesisData/Pb1/
            Pb1_PSD1_00'...
            num2str(j) '_ls_' num2str(i) '.dat']);
        hold_file2 = load(['/Users/LJBrandt/Documents/ThesisData/Pb1/
            Pb1_PSD2_00'...
            num2str(j) '_ls_' num2str(i) '.dat']);

        PSD0 = cat(1, PSD0, hold_file0);
        PSD1 = cat(1, PSD1, hold_file1);
        PSD2 = cat(1, PSD2, hold_file2);

    end
    PSD_Data{i} = [PSD0 PSD1 PSD2];
end

```

```

    end

    PSD0_Data{i+1} = PSD0;
    PSD1_Data{i+1} = PSD1;
    PSD2_Data{i+1} = PSD2;

end

clear Background_runs Fe_runs hold_file hold_file0 hold_file1 hold_file2
...
i j NaI NaI_channels neutron_channels Pb1_runs Pb3_runs PSD0 PSD1
PSD2
%%

%%%%%%%%%%%%%
% Import Background Data %
%%%%%%%%%%%%%

for i = 1: NaI_channels
    NaI = [];
    for j = 1: Background_runs

        hold_file = load(['/Users/LJBrandt/Documents/ThesisData/
Background/Background_PHA_00' ...
        num2str(j) '_ls_' num2str(i-1) '.dat']);
        NaI = cat(1, NaI, hold_file);

    end
    NaI_Data{i} = NaI;
end

for i = 0: neutron_channels-1

```

```

PSD0 = [];
PSD1 = [];
PSD2 = [];
for j = 1: Background_runs

    hold_file0 = load(['~/Users/LJBrandt/Documents/ThesisData/
        Background/Background_PSD0_00',...
        num2str(j) '_ls_' num2str(i) '.dat']);
    hold_file1 = load(['~/Users/LJBrandt/Documents/ThesisData/
        Background/Background_PSD1_00',...
        num2str(j) '_ls_' num2str(i) '.dat']);
    hold_file2 = load(['~/Users/LJBrandt/Documents/ThesisData/
        Background/Background_PSD2_00',...
        num2str(j) '_ls_' num2str(i) '.dat']);

    PSD0 = cat(1, PSD0, hold_file0);
    PSD1 = cat(1, PSD1, hold_file1);
    PSD2 = cat(1, PSD2, hold_file2);

end

PSD0_Data{i+1} = PSD0;
PSD1_Data{i+1} = PSD1;
PSD2_Data{i+1} = PSD2;

end

clear Background_runs Fe_runs hold_file hold_file0 hold_file1 hold_file2
...
i j NaI NaI_channels neutron_channels Pb1_runs Pb3_runs PSD0 PSD1
PSD2
%%
%%%%%%%%%%%%%
% Import 3 Block Lead Fission Data %

```

```

%%%%%%%%%%%%%%%
for i = 1: NaI_channels
    NaI = [];
    for j = 1: Pb3_runs
        hold_file = load(['/Users/LJBrandt/Documents/ThesisData/Pb3/
Pb3_PHA_00',...
        num2str(j) '_ls_' num2str(i-1) '.dat']);
        NaI = cat(1, NaI, hold_file);
    end
    NaI_Data{i} = NaI;
end

for i = 0: neutron_channels-1
    PSD0 = [];
    PSD1 = [];
    PSD2 = [];
    for j = 1: Pb3_runs
        hold_file0 = load(['/Users/LJBrandt/Documents/ThesisData/Pb3/
Pb3_PSD0_00',...
        num2str(j) '_ls_' num2str(i) '.dat']);
        hold_file1 = load(['/Users/LJBrandt/Documents/ThesisData/Pb3/
Pb3_PSD1_00',...
        num2str(j) '_ls_' num2str(i) '.dat']);
        hold_file2 = load(['/Users/LJBrandt/Documents/ThesisData/Pb3/
Pb3_PSD2_00',...
        num2str(j) '_ls_' num2str(i) '.dat']);
    end

```

```

PSD0 = cat(1, PSD0, hold_file0);
PSD1 = cat(1, PSD1, hold_file1);
PSD2 = cat(1, PSD2, hold_file2);

end

PSD0_Data{i+1} = PSD0;
PSD1_Data{i+1} = PSD1;
PSD2_Data{i+1} = PSD2;

end

clear Background_runs Fe_runs hold_file hold_file0 hold_file1 hold_file2
...
i j NaI NaI_channels neutron_channels Pb1_runs Pb3_runs PSD0 PSD1
PSD2

%%%%%%%%%%%%%
%%%%%%%%%%%%%
%Bethe Block Calculations
%%%%%%%%%%%%%
%%%%%%%%%%%%%
%%%%%%%%%%%%%
%Written by Maj Van Dyk
%Edited by Lt Brandt

%%%%%%%%%%%%%
%General Parameters
c = 2.99792458*10^8; %meters/sec
re = 2.817940325*10^(-13); %radius of an electron in centimeters
me = 0.510998918/c^2;%mass of an electron in MeV
Mpart = 105.658372/c^2; %mass of a muon in MeV
Na = 6.0221415*10^23;%Avagadros number

```

```

zpart = 1.;

%NaI Parameters
ZdivA = 0.42697;
rho = 3.667;%density of NaI=3.667 g/cm^3
Ionization = 452.*10^(-6); %MeV
thickness = 5.08;%cm
cbar = 6.0572;
a = 0.12516;
x1 = 3.5920;
smallk = 3.0398;

%Stainless Steel Parameters
ZdivA_SS = 0.46556;
rho_SS = 7.8740;
Ionization_SS = 286.*10^(-6); %MeV
thickness_SS_2 = 0.1016*2;%cm
thickness_SS_1 = 0.1016;%cm
cbar_SS = 4.2911;
a_SS = 0.14680;
x1_SS = 3.1531;
smallk_SS = 2.9632;

%Teflon Parameters
ZdivA_Teflon = 0.47992;
rho_Teflon = 2.2;
Ionization_Teflon = 99.1*10^(-6); %MeV
thickness_Teflon = 0.2159;%cm
cbar_Teflon = 3.4161;
a_Teflon = 0.10606;
x1_Teflon = 2.7404;
smallk_Teflon = 3.4046;

```

```

% dE1BB_NaI
% dE2BB_NaI
% dE3BB_NaI
% dE4BB_NaI

incr1 = 1;

for KEnergy1_iterate=140:1:5000

    %Find Emu2BB

    %Find decrease in energy due to NaI 1
    muon_energy=KEnergy1_iterate;
    vel=sqrt(-c^2*((1/(muon_energy/(Mpart*c^2)+1)^2)-1));
    gamma = 1/(sqrt(1 - (vel/c)^2));
    beta = vel/c;
    Tmax = (2*me*c^2*beta^2*gamma^2)/(1 + (2*gamma*me/Mpart)
        + (me/Mpart)^2);
    momen = Mpart*beta*gamma*c;
    frac = momen/(Mpart*c);
    x = log10(frac);
    densitycorrection = 2*log(10)*x - cbar + a*(x1 - x)^
        smallk;
    K = 4*pi*Na*re^2*me*c^2;
    dE1BB_NaI(incr1) = K*zpart^2*(ZdivA)*(1/beta^2)*((1/2)*
        log((2*me*c^2*beta^2*gamma^2*Tmax)/Ionization^2) -
        beta^2 - densitycorrection/2)*thickness*rho; %MeV

    KEnergy1_BB_NaI=KEnergy1_iterate-dE1BB_NaI(incr1);

```

```

%Find decrease in energy due to Teflon
muon_energy=KEnergy1_BB_NaI;
vel=sqrt(-c^2*((1/(muon_energy/(Mpart*c^2)+1)^2)-1));

gamma = 1/(sqrt(1 - (vel/c)^2));
beta = vel/c;
Tmax = (2*me*c^2*beta^2*gamma^2)/(1 + (2*gamma*me/Mpart)
+ (me/Mpart)^2);
momen = Mpart*beta*gamma*c;
frac = momen/(Mpart*c);
x = log10(frac);
densitycorrection = 2*log(10)*x - cbar_Teflon + a_Teflon
*(x1_Teflon - x)^smallk_Teflon;
K = 4*pi*Na*re^2*me*c^2;
dE1BB_Teflon_lower = K*zpart^2*(ZdivA_Teflon)*(1/beta^2)
*((1/2)*log((2*me*c^2*beta^2*gamma^2*Tmax)/
Ionization_Teflon^2) - beta^2 - densitycorrection/2)
*thickness_Teflon*rho_Teflon; %MeV

KEnergy1_BB_Teflon_lower=KEnergy1_BB_NaI-
dE1BB_Teflon_lower;

%Find decrease in energy due to Stainless Steel
muon_energy=KEnergy1_BB_Teflon_lower;
vel=sqrt(-c^2*((1/(muon_energy/(Mpart*c^2)+1)^2)-1));

gamma = 1/(sqrt(1 - (vel/c)^2));
beta = vel/c;
Tmax = (2*me*c^2*beta^2*gamma^2)/(1 + (2*gamma*me/Mpart)
+ (me/Mpart)^2);

```

```

momen = Mpart*beta*gamma*c;
frac = momen/(Mpart*c);
x = log10(frac);
densitycorrection = 2*log(10)*x - cbar_SS + a_SS*(x1_SS
- x)^smallk_SS;
K = 4*pi*Na*re^2*me*c^2;
dE1BB_SS = K*zpart^2*(ZdivA_SS)*(1/beta^2)*((1/2)*log
((2*me*c^2*beta^2*gamma^2*Tmax)/Ionization_SS^2) -
beta^2 - densitycorrection/2)*thickness_SS_2*rho_SS;
%MeV

KEnergy1_BB_SS=KEnergy1_BB_Teflon_lower-dE1BB_SS;

%Find decrease in energy due to Teflon
muon_energy=KEnergy1_BB_SS;
vel=sqrt((-c^2*((1/(muon_energy/(Mpart*c^2))+1)^2)-1));
gamma = 1/(sqrt(1-(vel/c)^2));
beta = vel/c;
Tmax = (2*me*c^2*beta^2*gamma^2)/(1+(2*gamma*me/Mpart)
+ (me/Mpart)^2);
momen = Mpart*beta*gamma*c;
frac = momen/(Mpart*c);
x = log10(frac);
densitycorrection = 2*log(10)*x - cbar_Teflon + a_Teflon
*(x1_Teflon - x)^smallk_Teflon;
K = 4*pi*Na*re^2*me*c^2;
dE2BB_Teflon_upper = K*zpart^2*(ZdivA_Teflon)*(1/beta^2)
*((1/2)*log((2*me*c^2*beta^2*gamma^2*Tmax)/
Ionization_Teflon^2) - beta^2 - densitycorrection/2)
*thickness_Teflon*rho_Teflon; %MeV

```

```

KEnergy2_BB=KEnergy1_BB_SS-dE2BB_Teflon_upper;

%find Emu3BB

%Find decrease in energy due to NaI 2
muon_energy=KEnergy2_BB;
vel=sqrt (-c^2*((1/(muon_energy/(Mpart*c^2)+1)^2)-1));
gamma = 1/(sqrt(1 - (vel/c)^2));
beta = vel/c;
Tmax = (2*me*c^2*beta^2*gamma^2)/(1 + (2*gamma*me/Mpart)
+ (me/Mpart)^2);
momen = Mpart*beta*gamma*c;
frac = momen/(Mpart*c);
x = log10(frac);
densitycorrection = 2*log(10)*x - cbar + a*(x1 - x) ^
smallk;
K = 4*pi*Na*re^2*me*c^2;
dE2BB_NaI(increl) = K*zpart^2*(ZdivA)*(1/beta^2)*((1/2)*
log((2*me*c^2*beta^2*gamma^2*Tmax)/Ionization^2) -
beta^2 - densitycorrection/2)*thickness*rho; %MeV

KEnergy2_BB_NaI=KEnergy2_BB-dE2BB_NaI(increl);

%Find decrease in energy due to Teflon
muon_energy=KEnergy2_BB_NaI;
vel=sqrt (-c^2*((1/(muon_energy/(Mpart*c^2)+1)^2)-1));

```

```

gamma = 1/(sqrt(1 - (vel/c)^2));
beta = vel/c;
Tmax = (2*me*c^2*beta^2*gamma^2)/(1 + (2*gamma*me/Mpart)
+ (me/Mpart)^2);
momen = Mpart*beta*gamma*c;
frac = momen/(Mpart*c);
x = log10(frac);
densitycorrection = 2*log(10)*x - cbar_Teflon + a_Teflon
*(x1_Teflon - x)^smallk_Teflon;
K = 4*pi*Na*re^2*me*c^2;
dE2BB_Teflon_lower = K*zpart^2*(ZdivA_Teflon)*(1/beta^2)
*((1/2)*log((2*me*c^2*beta^2*gamma^2*Tmax)/
Ionization_Teflon^2) - beta^2 - densitycorrection/2)
*thickness_Teflon*rho_Teflon; %MeV

KEnergy2_BB_Teflon_lower=KEnergy2_BB_NaI-
dE2BB_Teflon_lower;

%Find decrease in energy due to Stainless Steel
muon_energy=KEnergy2_BB_Teflon_lower;
vel=sqrt(-c^2*((1/(muon_energy/(Mpart*c^2)+1)^2)-1));

gamma = 1/(sqrt(1 - (vel/c)^2));
beta = vel/c;
Tmax = (2*me*c^2*beta^2*gamma^2)/(1 + (2*gamma*me/Mpart)
+ (me/Mpart)^2);
momen = Mpart*beta*gamma*c;
frac = momen/(Mpart*c);
x = log10(frac);
densitycorrection = 2*log(10)*x - cbar_SS + a_SS*(x1_SS

```

```

- x) ^ smallk_SS;

K = 4*pi*Na*re^2*me*c^2;
dE2BB_SS = K*zpart^2*(ZdivA_SS)*(1/beta^2)*((1/2)*log
((2*me*c^2*beta^2*gamma^2*Tmax)/Ionization_SS^2) -
beta^2 - densitycorrection/2)*thickness_SS_2*rho_SS;
%MeV

KEnergy2_BB_SS=KEnergy2_BB_Teflon_lower-dE2BB_SS;

%Find decrease in energy due to Teflon
muon_energy=KEnergy2_BB_SS;
vel=sqrt(-c^2*((1/(muon_energy/(Mpart*c^2)+1)^2)-1));

gamma = 1/(sqrt(1 - (vel/c)^2));
beta = vel/c;
Tmax = (2*me*c^2*beta^2*gamma^2)/(1 + (2*gamma*me/Mpart)
+ (me/Mpart)^2);
momen = Mpart*beta*gamma*c;
frac = momen/(Mpart*c);
x = log10(frac);
densitycorrection = 2*log(10)*x - cbar_Teflon + a_Teflon
*(x1_Teflon - x)^ smallk_Teflon;
K = 4*pi*Na*re^2*me*c^2;
dE3BB_Teflon_upper = K*zpart^2*(ZdivA_Teflon)*(1/beta^2)
*((1/2)*log((2*me*c^2*beta^2*gamma^2*Tmax)/
Ionization_Teflon^2) - beta^2 - densitycorrection/2)
*thickness_Teflon*rho_Teflon; %MeV

KEnergy3_BB=KEnergy2_BB_SS-dE3BB_Teflon_upper;

```

```

%find Emu4BB

%Find decrease in energy due to NaI 3

muon_energy= KEnergy3_BB;

vel=sqrt (-c^2*((1/(muon_energy/(Mpart*c^2)+1)^2)-1));

gamma = 1/(sqrt(1 - (vel/c)^2));
beta = vel/c;
Tmax = (2*me*c^2*beta^2*gamma^2)/(1 + (2*gamma*me/Mpart)
+ (me/Mpart)^2);
momen = Mpart*beta*gamma*c;
frac = momen/(Mpart*c);
x = log10(frac);
densitycorrection = 2*log(10)*x - cbar + a*(x1 - x) ^
smallk;
K = 4*pi*Na*re^2*me*c^2;
dE3BB_NaI(incr1) = K*zpart^2*(ZdivA)*(1/beta^2)*((1/2)*
log((2*me*c^2*beta^2*gamma^2*Tmax)/Ionization^2) -
beta^2 - densitycorrection/2)*thickness*rho; %MeV

KEnergy3_BB_NaI=KEnergy3_BB-dE3BB_NaI(incr1);

%Find decrease in energy due to Teflon

muon_energy=KEnergy3_BB_NaI;

vel=sqrt (-c^2*((1/(muon_energy/(Mpart*c^2)+1)^2)-1));

gamma = 1/(sqrt(1 - (vel/c)^2));
beta = vel/c;
Tmax = (2*me*c^2*beta^2*gamma^2)/(1 + (2*gamma*me/Mpart)
+ (me/Mpart)^2);
momen = Mpart*beta*gamma*c;

```

```

frac = momen/ (Mpart*c);
x = log10(frac);
densitycorrection = 2*log(10)*x - cbar_Teflon + a_Teflon
*(x1_Teflon - x)^smallk_Teflon;
K = 4*pi*Na*re^2*me*c^2;
dE3BB_Teflon_lower = K*zpart^2*(ZdivA_Teflon)*(1/beta^2)
*((1/2)*log((2*me*c^2*beta^2*gamma^2*Tmax)/
Ionization_Teflon^2) - beta^2 - densitycorrection/2)
*thickness_Teflon*rho_Teflon; %MeV

KEnergy3_BB_Teflon_lower=KEnergy3_BB_NaI-
dE3BB_Teflon_lower;

% Find decrease in energy due to Stainless Steel
muon_energy=KEnergy3_BB_Teflon_lower;
vel=sqrt(-c^2*((1/(muon_energy/(Mpart*c^2)+1)^2)-1));

gamma = 1/(sqrt(1 - (vel/c)^2));
beta = vel/c;
Tmax = (2*me*c^2*beta^2*gamma^2)/(1 + (2*gamma*me/Mpart)
+ (me/Mpart)^2);
momen = Mpart*beta*gamma*c;
frac = momen/ (Mpart*c);
x = log10(frac);
densitycorrection = 2*log(10)*x - cbar_SS + a_SS*(x1_SS
- x)^smallk_SS;
K = 4*pi*Na*re^2*me*c^2;
dE3BB_SS = K*zpart^2*(ZdivA_SS)*(1/beta^2)*((1/2)*log
((2*me*c^2*beta^2*gamma^2*Tmax)/Ionization_SS^2) -
beta^2 - densitycorrection/2)*thickness_SS_2*rho_SS;
%MeV

```

```

KEnergy3_BB_SS=KEnergy3_BB_Teflon_lower-dE3BB_SS;

%Find decrease in energy due to Teflon
muon_energy=KEnergy3_BB_SS;
vel=sqrt(-c^2*((1/(muon_energy/(Mpart*c^2)+1)^2)-1));

gamma = 1/(sqrt(1 - (vel/c)^2));
beta = vel/c;
Tmax = (2*me*c^2*beta^2*gamma^2)/(1 + (2*gamma*me/Mpart)
+ (me/Mpart)^2);
momen = Mpart*beta*gamma*c;
frac = momen/(Mpart*c);
x = log10(frac);
densitycorrection = 2*log(10)*x - cbar_Teflon + a_Teflon
*(x1_Teflon - x)^smallk_Teflon;
K = 4*pi*Na*re^2*me*c^2;
dE4BB_Teflon_upper = K*zpart^2*(ZdivA_Teflon)*(1/beta^2)
*((1/2)*log((2*me*c^2*beta^2*gamma^2*Tmax)/
Ionization_Teflon^2) - beta^2 - densitycorrection/2)
*thickness_Teflon*rho_Teflon; %MeV

```

KEnergy4_BB=KEnergy3_BB_SS-dE4BB_Teflon_upper;

```

%find muon exiting energy
%Find decrease in energy due to NaI 4
muon_energy= KEnergy4_BB;
vel=sqrt(-c^2*((1/(muon_energy/(Mpart*c^2)+1)^2)-1));

gamma = 1/(sqrt(1 - (vel/c)^2));
beta = vel/c;

```

```

Tmax = (2*me*c^2*beta^2*gamma^2) / (1 + (2*gamma*me/Mpart)
+ (me/Mpart)^2);

momen = Mpart*beta*gamma*c;
frac = momen/ (Mpart*c);
x = log10(frac);
densitycorrection = 2*log(10)*x - cbar + a*(x1 - x)^
smallk;

K = 4*pi*Na*re^2*me*c^2;
dE4BB_NaI(increl) = K*zpart^2*(ZdivA)*(1/beta^2)*((1/2)*
log((2*me*c^2*beta^2*gamma^2*Tmax)/Ionization^2) -
beta^2 - densitycorrection/2)*thickness*rho; %MeV

KEnergy4_BB_NaI=KEnergy4_BB-dE4BB_NaI(increl);

%Find decrease in energy due to Teflon

muon_energy=KEnergy4_BB_NaI;
vel=sqrt(-c^2*((1/(muon_energy/(Mpart*c^2)+1)^2)-1));

gamma = 1/(sqrt(1 - (vel/c)^2));
beta = vel/c;
Tmax = (2*me*c^2*beta^2*gamma^2) / (1 + (2*gamma*me/Mpart)
+ (me/Mpart)^2);
momen = Mpart*beta*gamma*c;
frac = momen/ (Mpart*c);
x = log10(frac);
densitycorrection = 2*log(10)*x - cbar_Teflon + a_Teflon
*(x1_Teflon - x)^smallk_Teflon;
K = 4*pi*Na*re^2*me*c^2;
dE4BB_Teflon_lower = K*zpart^2*(ZdivA_Teflon)*(1/beta^2)
*((1/2)*log((2*me*c^2*beta^2*gamma^2*Tmax)/
Ionization_Teflon^2) - beta^2 - densitycorrection/2)

```

```

*thickness_Teflon*rho_Teflon;    %MeV

KEnergy4_BB_Teflon_lower=KEnergy4_BB_NaI-
dE4BB_Teflon_lower;

% Find decrease in energy due to Stainless Steel
muon_energy=KEnergy4_BB_Teflon_lower;
vel=sqrt (-c^2*((1/(muon_energy/(Mpart*c^2)+1)^2)-1));
gamma = 1/(sqrt(1 - (vel/c)^2));
beta = vel/c;
Tmax = (2*me*c^2*beta^2*gamma^2)/(1 + (2*gamma*me/Mpart)
+ (me/Mpart)^2);
momen = Mpart*beta*gamma*c;
frac = momen/(Mpart*c);
x = log10(frac);
densitycorrection = 2*log(10)*x - cbar_SS + a_SS*(x1_SS
- x)^smallk_SS;
K = 4*pi*Na*re^2*me*c^2;
dE4BB_SS = K*zpart^2*(ZdivA_SS)*(1/beta^2)*((1/2)*log
((2*me*c^2*beta^2*gamma^2*Tmax)/Ionization_SS^2) -
beta^2 - densitycorrection/2)*thickness_SS_1*rho_SS;
%MeV

KEnergy_exit_BB(incr1)=KEnergy4_BB_Teflon_lower-dE4BB_SS
;

incr1=incr1+1;

end

```

```
%Save workspace as BetheBlock.mat

%MAIN PORTION OF CODE

%Performs Neutron Timing calculations
%and NaI muon energy determination

%Written by Maj Greg Van Dyk
%07 November 2013
%Edited by Lt Logan Brandt
%November 2014

close all
clear all
clc

% File Characteristics for input data

total_files_NaI=4;
total_files_neutrons=8;
concoident_acquisition_window=5000;
```

```

%Coincident window for neutron digitizers, take the time
%in nanoseconds divided by 4; 20 microsec=5000, 50 microsec=12500

%Initializations
counter=1;
counter1=1;
counter3=1;
counter5=1;
incr=1;
incrl=1;
energy4_exiting_hist=[];

progress=0;

%%%%%%%%%%%%%
%Import Data
%%%%%%%%%%%%%
load('Background_Data.mat') %%%% Change with new
material
load('Fe_Data.mat')
load('Pb1_Data.mat')
load('Pb2_Data.mat')
load('Pb3_Data.mat')

%%%%%%%%%%%%%
% Data Input for the Neutron Channels
%%%%%%%%%%%%%

%Import the first neutron digitizer from text files and load into
matrices
k=1;

```

```

for i=2:total_files_neutrons

    Data_neutrons1{i}=PSD0_Data{i};

    if numel(Data_neutrons1{i})>0
        PSD_neutrons1{k}=Data_neutrons1{i}(:,4);
        timing_neutrons1{k}=Data_neutrons1{i}(:,1);
        k=k+1;
    end
end

%Import the second neutron digitizer from text files and load into
matrices
k=1;
for i=2:total_files_neutrons

    Data_neutrons2{i}=PSD1_Data{i};

    if numel(Data_neutrons2{i})>0
        PSD_neutrons2{k}=Data_neutrons2{i}(:,4);
        timing_neutrons2{k}=Data_neutrons2{i}(:,1);
        k=k+1;
    end
end

%Import the third neutron digitizer from text files and load into
matrices
k=1;
for i=2:total_files_neutrons

    Data_neutrons3{i}=PSD2_Data{i};

```

```

if numel(Data_neutrons3{i})>0
    PSD_neutrons3{k}=Data_neutrons3{i}(:,4);
    timing_neutrons3{k}=Data_neutrons3{i}(:,1);
    k=k+1;
end
end

%%%%%%%%%%%%%
% Data input for NaI(Tl) detectors
%%%%%%%%%%%%%

%Import the NaI data from text files and load into matrices
for i=0:total_files_NaI-1
    j=i+1;
    Data{j}=NaI_Data{j};
    pulse_heights_NaI{j}=Data{j}(:,2);
    timing_NaI{j}=Data{j}(:,1);
end

%%%%%%%%%%%%%
%Datal Input for Frequency Generator
%%%%%%%%%%%%%

time_stamp1=PSD0_Data{1}(:,1);
check_size1=numel(time_stamp1);

time_stamp2=PSD1_Data{1}(:,1);
check_size2=numel(time_stamp2);

```

```

time_stamp3=PSD2_Data{1}(:,1);
check_size3=numel(time_stamp3);

display('Data Input Complete')

%%%%%%%%%%%%%
% Filtering the data to pull out just one single event per time stamp
for
% frequency generator channels
%%%%%%%%%%%%%

last_time_stamp1=time_stamp1(1);
filtered_time_stamps1(1)=time_stamp1(1);
incr=2;
counter=1;

for m=2:check_size1
    current_time_stamp1=time_stamp1(m);
    timing_diff1=current_time_stamp1-last_time_stamp1;

    if abs(timing_diff1)>concurrent_acquisition_window
        filtered_time_stamps1(incr)=current_time_stamp1;
        incr=incr+1;
    end

    last_time_stamp1=time_stamp1(m);
end

```

```

last_time_stamp2=time_stamp2(1);
filtered_time_stamps2(1)=time_stamp2(1);
incr=2;

for m=2:check_size2
    current_time_stamp2=time_stamp2(m);
    timing_diff2=current_time_stamp2-last_time_stamp2;

    if abs(timing_diff2)>concurrent_acquisition_window
        filtered_time_stamps2(incr)=current_time_stamp2;
        incr=incr+1;
    end

    last_time_stamp2=time_stamp2(m);

end

last_time_stamp3=time_stamp3(1);
filtered_time_stamps3(1)=time_stamp3(1);
incr=2;

for m=2:check_size3
    current_time_stamp3=time_stamp3(m);
    timing_diff3=current_time_stamp3-last_time_stamp3;

    if abs(timing_diff3)>concurrent_acquisition_window
        filtered_time_stamps3(incr)=current_time_stamp3;
        incr=incr+1;
    end

    last_time_stamp3=time_stamp3(m);

```

```

end

filtered_time_stamps_trans1=transpose(filtered_time_stamps1);
filtered_time_stamps_trans2=transpose(filtered_time_stamps2);
filtered_time_stamps_trans3=transpose(filtered_time_stamps3);

total_triggers_neutrons=[numel(filtered_time_stamps1) ...
    numel(filtered_time_stamps2) numel(filtered_time_stamps3)];

minimum_triggers_neutrons=min(total_triggers_neutrons);

display('Function Generator Time Stamps Filtered')

%%%%%%%%%%%%%%%
% Filtering neutron datasets to pull out the correct PSD value
%%%%%%%%%%%%%%%

%Only look at neutron events for first digitizer
incr2=1;

for i=1:numel(PSD_neutrons1)

    for incr1=1:numel(PSD_neutrons1{i})

        if PSD_neutrons1{i}(incr1)>=0.1 && PSD_neutrons1{i}(incr1)<=0.3
            time_stamp_neutrons1(incr2)=timing_neutrons1{i}(incr1);
            neutrons1(incr2)=PSD_neutrons1{i}(incr1);

        incr2=incr2+1;
    end
end

```

```

    end
end

time_stamp_neutrons1_trans=transpose(time_stamp_neutrons1);
neutrons1_trans=transpose(neutrons1);

%Only look at neutron events for second digitizer
incr2=1;

for i=1:numel(PSD_neutrons2)

    for incr1=1:numel(PSD_neutrons2{i})

        if PSD_neutrons2{i}(incr1)>=0.1 && PSD_neutrons2{i}(incr1)<=0.3
            time_stamp_neutrons2(incr2)=timing_neutrons2{i}(incr1);
            neutrons2(incr2)=PSD_neutrons2{i}(incr1);

        incr2=incr2+1;
    end
end

time_stamp_neutrons2_trans=transpose(time_stamp_neutrons2);
neutrons2_trans=transpose(neutrons2);

%Only look at neutron events for third digitizer
incr2=1;

for i=1:numel(PSD_neutrons3)

    for incr1=1:numel(PSD_neutrons3{i})

```

```

if PSD_neutrons3{i}(incr1)>=0.1 && PSD_neutrons3{i}(incr1)<=0.3
    time_stamp_neutrons3(incr2)=timing_neutrons3{i}(incr1);
    neutrons3(incr2)=PSD_neutrons3{i}(incr1);

    incr2=incr2+1;
end
end
end

time_stamp_neutrons3_trans=transpose(time_stamp_neutrons3);
neutrons3_trans=transpose(neutrons3);

display('PSD Values Obtained')

%%%%%%%%%%%%%
% Compare frequency generator time stamps to neutron event time stamps
% Prevent neutron data stamps to be applied to incorrect time stamps
% due to clock turnover
%%%%%%%%%%%%%

time_between_neutron_events1=0;
old_timeindex_of_neutrons1=0;

for incr=1:numel(time_stamp_neutrons1)

    for i=1:numel(filtered_time_stamps1)

        timing_difference_NaI_neutrons1=time_stamp_neutrons1(incr)-
            filtered_time_stamps1(i);
        time_between_neutron_events1=abs(i-old_timeindex_of_neutrons1);
    end
end

```

```

if abs(timing_difference_NaI_neutrons1)<=
concurrent_acquisition_window
    timeindex_of_neutrons1(incr)=i;
    old_timeindex_of_neutrons1=i;
    break
end

end

display('Absolute Time Stamps of Neutrons1 Determined')

time_between_neutron_events2=0;
old_timeindex_of_neutrons2=0;

for incr=1:numel(time_stamp_neutrons2)

    for i=1:numel(filtered_time_stamps2)

        timing_difference_NaI_neutrons2=time_stamp_neutrons2(incr)-
            filtered_time_stamps2(i);
        time_between_neutron_events2=abs(i-old_timeindex_of_neutrons2);

        if abs(timing_difference_NaI_neutrons2)<=
        concurrent_acquisition_window
            timeindex_of_neutrons2(incr)=i;
            old_timeindex_of_neutrons2=i;
            break
        end
    end
end

```

```

    end
end

display('Absolute Time Stamps of Neutrons2 Determined')

time_between_neutron_events3=0;
old_timeindex_of_neutrons3=0;

for incr=1:numel(time_stamp_neutrons3)

    for i=1:numel(filtered_time_stamps3)

        timing_difference_NaI_neutrons3=time_stamp_neutrons3(incr)-
            filtered_time_stamps3(i);
        time_between_neutron_events3=abs(i-old_timeindex_of_neutrons3);

        if abs(timing_difference_NaI_neutrons3)<=
            coincident_acquisition_window
            timeindex_of_neutrons3(incr)=i;
            old_timeindex_of_neutrons3=i;
            break
        end

    end
end

display('Absolute Time Stamps of Neutrons3 Determined')
%
```

```

% Combine all neutron events time stamps into one vector
%%%%%%%%%%%%%%%
timeindex_of_neutrons1_trans=transpose(timeindex_of_neutrons1);
timeindex_of_neutrons2_trans=transpose(timeindex_of_neutrons2);
timeindex_of_neutrons3_trans=transpose(timeindex_of_neutrons3);

total_neutron_indexes=vertcat(timeindex_of_neutrons1_trans, ...
timeindex_of_neutrons2_trans,timeindex_of_neutrons3_trans);

%%
%%%%%%%%%%%%%%%
%Save previous section workspace as 'Material'_Run_Neutron_Timing
%This allows the energy determination section to be ran multiple
%times without having to rerun the nutrion timing section.

%%%%%%%%%%%%%%%
% clear;
% load('Pb3_Run_Neutron_Timing');
% clc;

%%%%%%%%%%%%%%%
% Begin NaI(Tl) energy determination
%%%%%%%%%%%%%%%
%%%%%%%%%%%%%%%
% Load Bethe Bloch Calculation Data
%%%%%%%%%%%%%%%
load('BetheBlock.mat');


```

```

counter = 1;
counter1 = 1;

%%%%%%%%%%%%%
% NaI(Tl) detector calibration data
%%%%%%%%%%%%%

%Used Cs-137 and Co-60 peaks for calibration

energy_NaI_cal = [0.662, 1.173, 1.333, 24.297];
MIP = [9910, 9459, 8844, 11489];

%%%%%%%%%%%%%
% 15 Jan %
%%%%%%%%%%%%%

channel_NaI_cal{1} = [409, 722, 814, MIP(1)];
channel_NaI_cal{2} = [372, 641, 728, MIP(2)];
channel_NaI_cal{3} = [312, 542, 609, MIP(3)];
channel_NaI_cal{4} = [735, 1271, 1439, MIP(4)];

pulse_height = cell2mat(pulse_heights_NaI);
pulse_height(pulse_height > 1.8*10^4 | pulse_height < 0) = NaN;
[r,c] = find(isnan(pulse_height));
pulse_height(r,:) = 0;

for i = 1:4

    Calibration{i} = polyfit(channel_NaI_cal{i}, energy_NaI_cal, 1);

```

```

NaI.energy(:,i) = pulse_height(:,i)*Calibration{i}(1) +
    Calibration{i}(2);

end

%%%%%%%%%%%%%
%Histogram of Landau Distribution (Energy Deposited in each NaI(Tl))
%%%%%%%%%%%%%

figure
for i = 1:4

    subplot(2,2,i)
    hist(NaI.energy(:,i), [0:1:60])
    %
    ylim([0,1000])
    xlim([0,50])
    title(['NaI(Tl) ' num2str(i)], 'FontSize', 30.)
    xlabel('Energy Deposited', 'FontSize', 30.)
    ylabel('Counts', 'FontSize', 30.)
    set(gca, 'FontSize', 20)
end

%
%%%%%%%%%%%%%
% Determine Limits to Muon Energy From Deposited Energy
%
%%%%%%%%%%%%%

lowest_energy=24.297 * 0.96; % MIP 24.297
upper_energy_detectors123=31.7466 * 1.12; %highest value for 5 GeV

```

```

muon=31.7466

upper_energy_detector4=31.7466 * 1.12;

for m=1:minimum_triggers_neutrons

% Set the energy deposited by the muon

energy1_interp= NaI_energy(m,1);
energy2_interp= NaI_energy(m,2);
energy3_interp= NaI_energy(m,3);
energy4_interp= NaI_energy(m,4);

if energy1_interp<=upper_energy_detectors123 && energy2_interp<=
upper_energy_detectors123...
&& energy3_interp<=upper_energy_detectors123 &&
energy4_interp<=upper_energy_detector4...
&& energy1_interp>=lowest_energy && energy2_interp>=
lowest_energy...
&& energy3_interp>=lowest_energy && energy4_interp>=
lowest_energy

%
%%%%%%%%%%%%%%%
%Count all neutrons for that muon event.
%
%%%%%%%%%%%%%%%

```

```

neutrons=0;

for j=1:numel(total_neutron_indexes)
    if m==total_neutron_indexes(j)
        neutrons=neutrons+1;
    end
end

%Find Chi^2
chi2=((dE1BB_NaI-energy1_interp).^2./dE1BB_NaI)+...
((dE2BB_NaI-energy2_interp).^2./dE2BB_NaI)+...
((dE3BB_NaI-energy3_interp).^2./dE3BB_NaI)+...
((dE4BB_NaI-energy4_interp).^2./dE4BB_NaI);

chi2_list=transpose(vertcat(chi2, KEnergy_exit_BB));

%Determine the Lowest Chi^2
if chi2~=0

[chi2_min,index]=min(chi2_list(:,1));
chi_list(counter1)=chi2_min;

KEnergy_exit=chi2_list(index,2);

%Determine the exiting energy
energy4_exiting_list(counter1)=KEnergy_exit;
energy4_exiting_hist=[energy4_exiting_hist,KEnergy_exit];
];

```

```

neutrons_list(counter1)=neutrons;

counter1=counter1+1;

end

end

%View Progress Through Files and clear chi2 for next file

counter=counter+1;
disp(counter)
chi2=0;
incr1=1;
chi2_list=[];

end

energy4_exiting_list_trans=transpose(energy4_exiting_list);
neutrons_list_trans=transpose(neutrons_list);

NeutronDataFile='NeutronDataFile.txt';
M=[energy4_exiting_list_trans neutrons_list_trans ];
dlmwrite(NeutronDataFile,M,'delimiter','\t','precision','%15.10f')

%%%%%%%%%%%%%
%%%%%%%%%%%%%
%ANALYSIS portion of code

```

```

%%%%%%%%%%%%%%%
%%%%%%%%%%%%%%%
%Written by 2Lt Logan Brandt

clear;
clc;
close all;

%%%%Index m =           1           2           3           4
Material = cellstr({'BackgroundF', 'FeF', 'Pb1F', 'Pb3F'});
Color = cellstr({'k', 'b', 'r', 'g'});
Material_Name = cellstr({'Background', '15 cm Iron', '5 cm Lead', '15 cm
Lead'});

bins = 0:40;
centers = {[0:100:5000], [0:1:30]};

for m = 1:length(Material)

%%%%%%%%%%%%%%%
%Load Data
%%%%%%%%%%%%%%%
Data{m} = load([Material{m} '_NeutronDataFile.txt']);
Muon_Energy{m} = Data{m}(:,1);
Neutron_Count{m} = Data{m}(:,2);
Total_Neutrons{m} = sum(Neutron_Count{m});
Total_Muons{m} = length(Muon_Energy{m});

```

```

%%%%%%%%%%%%%%%
%Muon Energy Distribution
%%%%%%%%%%%%%%%
Energy_Hist{m} = hist(Muon_Energy{m}, centers{1});
Mean_Muon_Energy{m} = mean(Muon_Energy{m});
Mode_Muon_Energy{m} = mode(Muon_Energy{m});

%%%%%%%%%%%%%%%
%Neutron Muon Energy Dependence
%%%%%%%%%%%%%%%
Hist2d{m} = hist3(Data{m}, 'Ctrs', centers, 'FaceColor', Color{m});

for r = 1:length(centers{1})
    Average_Neutrons_per_Energy{m}(r) = 0;

    for c = 1:length(centers{2})
        Average_Neutrons_per_Energy{m}(r) =
            Average_Neutrons_per_Energy{m}(r) + Hist2d{m}(r,c)*(c-1);

    end

    Neutrons_per_Energy{m}(r) = Average_Neutrons_per_Energy{m}(r);
    Muons_per_Energy{m}(r) = sum(Hist2d{m}(r,:));
    Average_Neutrons_per_Energy{m}(r) = Neutrons_per_Energy{m}(r)/
        Muons_per_Energy{m}(r);
    Average_Neutrons_per_Energy_Error{m}(r) = sqrt((sqrt(
        Neutrons_per_Energy{m}(r))/Neutrons_per_Energy{m}(r))^2 ...
        + (sqrt(Muons_per_Energy{m}(r))/Muons_per_Energy{m}(r))^2) *
        Average_Neutrons_per_Energy{m}(r);
end

```

```

end

for c = 1:length(centers{2})

    Muons_per_Neutron_Count{m}(c) = sum(Hist2d{m}(:,c));
    Energy_Spectrum_per_Neutron_Count{m}(c,:) = Hist2d{m}(:,c);

end

%%%%%%%%%%%%%
%Bin Neutrons
%%%%%%%%%%%%%

for i = 0:40
    Hist{m}(i+1) = sum(Neutron_Count{m} ==i);
end

Hist{m} = transpose(Hist{m});

%%%%%%%%%%%%%
%Remove Background
%%%%%%%%%%%%%

Hist_above_Background{m} = Hist{m} - Hist{1};
Hist_above_Background{m}(Hist_above_Background{m}(:) < 0) = 0;
Muons_above_Background{m} = sum(Hist_above_Background{m});
Neutrons_above_Background{m} = 0;
for i = 0:40
    Neutrons_above_Background{m} = Neutrons_above_Background{m} +
        Hist_above_Background{m}(i+1)*i;
end

```

```

%%%%%%%%%%%%%%%
%Find Results and error to produce specific number of neutrons
%%%%%%%%%%%%%%%

%Probability

Probability{m} = Hist_above_Background{m}./Muons_above_Background{m}
};

Prob_Error{m}=sqrt((sqrt(Hist_above_Background{m}) /
Hist_above_Background{m})^2 ...
+ (sqrt(Muons_above_Background{m}) /Muons_above_Background{m})^2)
*Probability{m};

%Average Neutrons produced found from total numbers

Average_Neutrons{m} = Total_Neutrons{m}/Total_Muons{m};
Average_Neutrons_Error{m} = sqrt((sqrt(Total_Neutrons{m}) /
Total_Neutrons{m})^2 ...
+ (sqrt(Total_Muons{m}) /Total_Muons{m})^2)*Average_Neutrons{m};

%Expectation value for the neutron count per muon found with
background

%removed

Neutrons_per_Muon{m} = Neutrons_above_Background{m} /
Muons_above_Background{m};
Neutrons_per_Muon_Error{m} = sqrt((sqrt(Neutrons_above_Background{m}
)) /Neutrons_above_Background{m})^2 ...
+ (sqrt(Muons_above_Background{m}) /Muons_above_Background{m})^2)
*Neutrons_per_Muon{m};

end

```

```

%%
for m = 1:length(Material)
    for i = 1: length(Average_Neutrons_per_Energy{m})
        h0(m,i) = ttest(Average_Neutrons_per_Energy{m}(i)-
            Average_Neutrons_per_Energy{1}(i));
    end

    MeV_Avg{m} = (Average_Neutrons_per_Energy{m}(2) +
        Average_Neutrons_per_Energy{m}(3))/2;
    GeV_Avg{m} = (Average_Neutrons_per_Energy{m}(20) +
        Average_Neutrons_per_Energy{m}(21))/2;

    MeV_Avg_Error{m} = (Average_Neutrons_per_Energy_Error{m}(2) +
        Average_Neutrons_per_Energy_Error{m}(3))/2;
    GeV_Avg_Error{m} = (Average_Neutrons_per_Energy_Error{m}(20) +
        Average_Neutrons_per_Energy_Error{m}(21))/2;
end

for m = 2: length(Material)
    MeV_Avg{m} = MeV_Avg{m} - MeV_Avg{1};
    GeV_Avg{m} = GeV_Avg{m} - GeV_Avg{1};
end

%%
%%%%%%%%%%%%%
%T-Tests comparing data sets
%%%%%%%%%%%%%

```

```

[h1,pPb1Pb3] = ttest2(Hist_above_Background{3}, Hist_above_Background
{4})

[h2,pFePb3] = ttest2(Hist_above_Background{2}, Hist_above_Background{4})
[h3,pFePb1] = ttest2(Hist_above_Background{2}, Hist_above_Background{3})

[h1,pBkgFe] = ttest2(Hist_above_Background{1}, Hist_above_Background{2})
[h2,pBkgPb1] = ttest2(Hist_above_Background{1}, Hist_above_Background
{3})
[h3,pBkgPb3] = ttest2(Hist_above_Background{1}, Hist_above_Background
{4})

%%

[h1,pPb1Pb3] = ttest2(Average_Neutrons_per_Energy{3},
Average_Neutrons_per_Energy{4})

[h2,pFePb3] = ttest2(Average_Neutrons_per_Energy{2},
Average_Neutrons_per_Energy{4})

[h3,pFePb1] = ttest2(Average_Neutrons_per_Energy{2},
Average_Neutrons_per_Energy{3})

[h1,pBkgFe] = ttest2(Average_Neutrons_per_Energy{1},
Average_Neutrons_per_Energy{2})

[h2,pBkgPb1] = ttest2(Average_Neutrons_per_Energy{1},
Average_Neutrons_per_Energy{3})

[h3,pBkgPb3] = ttest2(Average_Neutrons_per_Energy{1},
Average_Neutrons_per_Energy{4})

%%

%%%%%%%%%%%%%
%Plot raw neutron counts per muon event
%%%%%%%%%%%%%
figure(1)

```

```

groupplot= horzcat(Hist{1:length(Material)});  

Neutron_Histogram = bar(bins, [groupplot], 'grouped');  

xlim([-1,21])  

for m = 1:length(Material)  

    set(Neutron_Histogram(m), 'FaceColor', Color{m}, 'EdgeColor', Color  

        {m});  

end  

legend(Material.Name)  

xlabel('Neutron Counts per Muon', 'FontSize', 30.)  

ylabel('Muon Events', 'FontSize', 30.)  

set(gca, 'FontSize', 20)  

%%  

%%%%%  

%Plot Neutron Counts with Background Removed  

%%%%%  

figure(2)  

groupplot= horzcat( Hist_above_Boundary{2:length(Material)});  

Neutron_Histogram_wo_Boundary = bar(bins, [groupplot], 'grouped');  

xlim([-1,21])  

for m = 2:length(Material)  

    set(Neutron_Histogram_wo_Boundary(m-1), 'FaceColor', Color{m}, '  

        EdgeColor', Color{m});  

end  

legend(Material.Name{2:length(Material.Name)})  

xlabel('Neutron Counts per Muon', 'FontSize', 30.)  

ylabel('Muon Events', 'FontSize', 30.)  

set(gca, 'FontSize', 20)

```

```

%%

%%%%%%%%%%%%%%%
%Plot Probability Distribution with Error Bars
%%%%%%%%%%%%%%%

figure(3)

for m = 2:length(Material)
    Poisson_plot{m} = plot(bins,poisspdf(bins, Neutrons_per_Muon{m}),
                           Color{m});
    Prob_Plot{m} = errorbar(bins, Probability{m}, Prob_Error{m},
                           Color{m}, 'MarkerSize', 10);
end
hold all
poissfit(Probability{m})
xlim([-1,21])
ylim([0,.25])
legend(Material_Name{2:length(Material_Name)})
xlabel('Neutrons Produced per Muon','FontSize',30.)
ylabel('Probability','FontSize',30.)
set(gca, 'FontSize', 20)

%%

%%%%%%%%%%%%%%%
%Plot Neutron counts against Muon Energy
%%%%%%%%%%%%%%%

figure(5)

for m = 1:length(Material)

```

```

    subplot(2,2,m)
    scatter(Muon_Energy{m}, Neutron_Count{m}, '.', 'MarkerEdgeColor', Color
    {m}...
    , 'MarkerFaceColor', Color{m}, 'SizeData', 250);
    title(Material.Name{m}, 'FontSize', 30.)
    xlim([0,3000])
    xlabel('Muon Energy [MeV]', 'FontSize', 30.)
    ylim([0,30])
    ylabel('Neutron Counts', 'FontSize', 30.)
    hold on
    set(gca, 'FontSize', 20)

end

%%

%Neutron Yield for each 100 MeV incident muon energy bin

figure(6)

for m = 1:length(Material)

    subplot(2,2,m)
    bar(centers{1}, Average_Neutrons_per_Energy{m} , 'FaceColor', Color{
    m}, ...
    'EdgeColor', Color{m});
    ylim([0,10])
    xlim([0,3000])
    title(Material.Name{m}, 'FontSize', 30.)
    xlabel('Muon Energy [MeV]', 'FontSize', 30.)
    ylabel('Average Neutron Counts', 'FontSize', 20.)

```

```

set(gca, 'FontSize', 20)

end

%%

%%%%%%%%%%%%%
%Incident Muon Energy Distribution
%%%%%%%%%%%%%

figure(7)

for m = 1:length(Material)

    subplot(2,2,m)
    bar(centers{1}, Energy_Hist{m}, 'FaceColor', Color{m}, 'EdgeColor',
        Color{m});
    ylim([0,4000])
    xlim([0,3000])
    title(Material.Name{m}, 'FontSize', 30.)
    xlabel('Muon Energy [MeV]', 'FontSize', 30.)
    ylabel('Muon Counts', 'FontSize', 30.)
    set(gca, 'FontSize', 20)

end

%%

%%%%%%%%%%%%%
%Plot Average Neutron Yield with Error
%%%%%%%%%%%%%

```

```

figure(8)

for m = 1:length(Material)
    Avg_Energy_Plot{m} = errorbar(centers{1},
        Average_Neutrons_per_Energy{m}, ...
        Average_Neutrons_per_Energy_Error{m}, Color{m}, 'MarkerSize'
        , 10);
    hold all
end

xlim([0,3000])
ylim([0,10])
legend(Material_Name{1:length(Material_Name)})
xlabel('Incident Muon Energy [MeV]', 'FontSize', 30.)
ylabel('Average Neutron Counts', 'FontSize', 30.)
set(gca, 'FontSize', 20)

%%

%%%%%
%Plot Muon Energy Spectrum for a Given Neutron Yield
%%%%%
Neutron_Count_Analyzed = 4;
% figure(9)

for neutrons = 1: Neutron_Count_Analyzed
    subplot(2,2,neutrons)
    for m = 1:length(Material)
        Energy_Spectrum_per_Neutron_Count_Plot{m} = plot(centers{1},
            ...
            Energy_Spectrum_per_Neutron_Count{m}(neutrons,:), Color{
            m}, 'MarkerSize', 10);
        hold all
    end
    xlim([0,3000])

```

```
legend(Material_Name{1:length(Material_Name)})  
title(['Neutron Yield of ' num2str(neutrons-1) ' Neutrons'], '  
FontSize', 30.)  
xlabel('Incident Muon Energy [MeV]', 'FontSize', 25.)  
ylabel('Muon Counts', 'FontSize', 30.)  
set(gca, 'FontSize', 20)  
end
```

Bibliography

1. G. K. VanDyk, “Muon Concentration and Moderation to Study Muon Catalyzed Fusion in a Deuterium Gas Multiwire Proportional Counter,” 2013.
2. K. Nagamine, *Introductory Muon Science*. New York: Cambridge University Press, 2003.
3. H. K. M. Tanaka and et al., “Radiographic Imaging Below a Volcanic Crater Floor with Cosmic-Ray Muons,” *American Journal of Science*, vol. 308, p. 843, 2008.
4. e. a. L. W. Alvarez, “Search for Hidden Chambers in the Pyramids,” *Science*, vol. 167, 1970.
5. S. Pesente and et al., “First Results on Material Identification and Imaging with a Large-volume Muon Tomography Prototype,” *IEEE*, 2009.
6. D. Schwellenbach and et al., “Passive Imaging of Warhead-Like Configurations with Cosmic Ray Muon Tracking Scanners,” 2013.
7. K. Miyadera and et al., “Imaging Fukushima Daiichi Reactors with Muons,” *AIP Advances*, vol. 3 no. 052133, 2013.
8. J. Perry and et al., “Imaging a nuclear reactor using cosmic ray muons,” *Journal of Applied Physics*, vol. 113, no. 184909, 2013.
9. M. Benettoni and et al., “Muon Radiography with the CMS Muon Barrel Chambers,” *IEEE Nuclear Science Symposium Conference Record*, vol. N19-4, 2007.
10. “Decision Sciences: Introducing the Multi-Mode Passive Detection System (MM-PDS),” 2013.
11. “Some Consequences of the Electromagnetic Interaction between mu-Mesons and Nuclei,” *Review of Modern Physics*, vol. 21, p. 133, 1949.
12. V. Oberacker, “Prompt muon-induced fission: a probe for nuclear energy dissipation,” *Acta Physica Hungarica New Series-Heavy Ion Physics*, vol. 10, pp. 221–230, 1999.
13. J. Maruhn, V. Oberacker, and V. Maruhn-Rezwani, “Muon-Induced Fission as a Probe for Fission Dynamics,” *Phys.Rev.Lett.*, vol. 44, pp. 1576–1579, 1980.
14. J. Perry, “Advanced Applications of Cosmic-ray Muon Radiography,” 2013.
15. V. E. Oberacker and et al., “Prompt muon-induced fission: a sensitive probe for nuclear energy dissipation and fission dynamics,” 2014.

16. N. C. Mukhopadhyay, “Nuclear Muon Capture,” *Physics Reports*, vol. 30, no. 1, p. 144, 1976.
17. D. V. Balin and et al., “High Precision Study of Muon Catalyzed Fusion in D2 and HD Gas,” *Physics of Particles and Nuclei*, vol. 42, no. 2, p. 185, 2011.
18. L. I. Ponomarev, “Muon Catalysed Fusion,” *Contemporary Physics*, vol. 31, no. 4, p. 219, 1990.
19. F. C. Frank, “Hypothetical Alternative Energy Sources for the Second Meson Events,” *Nature*, vol. 160, p. 525, 1947.
20. R. M. Kulsrud, “Cold Fusion Catalyzed by Muons and Electrons,” 1990.
21. C. J. Bridgman, *Introduction to the Physics of Nuclear Weapons*. DTRA, 2001.
22. C. H. Luu, T, “Neutron Production by Muon Spallation I: Theory,” *Lawrence Livermore National Laboratory*, 2006.
23. L. Reichhart and et al., “Measurement and simulation of the muon-induced neutron yield in lead,” *Astroparticle Physics*, vol. 47, 2013.
24. G. Knoll, *Radiation Detection and Measurement*. Hoboken, New Jersey: John Wiley and Sons, Inc., 2010.
25. D. Groom and et al., “Muon Stopping Power and Range Tables 10 MeV-100TeV,” *Atomic Data and Nuclear Data Tables*, vol. 76, no. 2, p. 1, 2001.
26. R. Sternheimer and et al., “Density Effect for the Ionization Loss of Charged Particles in Various Substances,” *Atomic Data and Nuclear Data Tables*, vol. 30, no. 2, p. 261, 1984.
27. E. Aguayo and et al., “Cosmic Ray Interactions in Shielding Materials ,” 2011.

REPORT DOCUMENTATION PAGE

*Form Approved
OMB No. 0704-0188*

The public reporting burden for this collection of information is estimated to average 1 hour per response, including the time for reviewing instructions, searching existing data sources, gathering and maintaining the data needed, and completing and reviewing the collection of information. Send comments regarding this burden estimate or any other aspect of this collection of information, including suggestions for reducing this burden to Department of Defense, Washington Headquarters Services, Directorate for Information Operations and Reports (0704-0188), 1215 Jefferson Davis Highway, Suite 1204, Arlington, VA 22202-4302. Respondents should be aware that notwithstanding any other provision of law, no person shall be subject to any penalty for failing to comply with a collection of information if it does not display a currently valid OMB control number. PLEASE DO NOT RETURN YOUR FORM TO THE ABOVE ADDRESS.

1. REPORT DATE (DD-MM-YYYY) 26-03-2015	2. REPORT TYPE Master's Thesis	3. DATES COVERED (From — To) Sept 2013 — Mar 2015		
4. TITLE AND SUBTITLE Analysis of Muon Induced Neutrons in Detecting High Z Nuclear Materials		5a. CONTRACT NUMBER 5b. GRANT NUMBER 5c. PROGRAM ELEMENT NUMBER		
6. AUTHOR(S) Brandt, Logan J, 2nd LT, USAF		5d. PROJECT NUMBER 5e. TASK NUMBER 5f. WORK UNIT NUMBER		
7. PERFORMING ORGANIZATION NAME(S) AND ADDRESS(ES) Air Force Institute of Technology Graduate School of Engineering and Management (AFIT/EN) 2950 Hobson Way WPAFB OH 45433-7765		8. PERFORMING ORGANIZATION REPORT NUMBER AFIT-ENP-MS-15-M-109		
9. SPONSORING / MONITORING AGENCY NAME(S) AND ADDRESS(ES) Air Force Office of Scientific Research AFOSR/RTB 801 North Randolph Street Arlington VA 22203-1977		10. SPONSOR/MONITOR'S ACRONYM(S) AFOSR		
		11. SPONSOR/MONITOR'S REPORT NUMBER(S)		
12. DISTRIBUTION / AVAILABILITY STATEMENT Distribution Statement A: Approved for Public Release; Distribution Unlimited				
13. SUPPLEMENTARY NOTES This work is declared a work of the U.S. Government and is not subject to copyright protection in the United States.				
14. ABSTRACT Simulations of muon interactions with high Z material using two different muon energies, 100 MeV and 1 GeV, were performed on five different materials of various atomic numbers yielding average neutron production rates that range from 2.3 ± 0.01 in enriched uranium to negligible amounts in aluminum when exposed to the 100 MeV energy muons. As the muon energy was increased to 1 GeV, neutron yields shrank to negligible levels. Little difference was found in neutron yield produced in non-fissile material. Experimental data was collected by exposing a 15 cm thick block of iron, and 5 and 15 cm thick blocks of lead to the natural atmospheric muon flux. The incident muon energy distribution was found to have a mode of 180 MeV and a mean of 520 MeV. Probability distributions were constructed for the neutron yields of each incident muon and no difference was found in the various distributions. The average muon induced neutron yield was also calculated and found to be 3.4 ± 0.1 for a 15 cm thick block of iron, 2.8 ± 0.1 for a 5 cm thick block of lead, and 2.2 ± 0.1 for a 15 cm thick block of lead.				
15. SUBJECT TERMS Nuclear Material Detection, Muon Imaging, Muons, Muon Spectrometry				
16. SECURITY CLASSIFICATION OF:		17. LIMITATION OF ABSTRACT UU	18. NUMBER OF PAGES 113	19a. NAME OF RESPONSIBLE PERSON Dr. Larry W. Burggraf, PhD, AFIT/ENP
a. REPORT	b. ABSTRACT			c. THIS PAGE